Astronomy 233 Winter 2009

Physical Cosmology

Week 10

Simulations and Semi-Analytic Models

Joel Primack

University of California, Santa Cruz

Cosmological Simulation Methods

Dissipationless Simulations

Particle-Particle (PP) - Aarseth NbodyN, N=1,...,6
Particle Mesh (PM) - see Klypin & Holtzman 1997
Adaptive PM (P3M) - Efstathiou et al.
Tree - Barnes & Hut 1986, PKDGRAV Stadel
TreePM - GADGET2, Springel 2005
Adaptive Mesh Refinement (AMR) - Klypin (ART)

Hydrodynamical Simulations

Fixed grid - Cen & Ostriker
Smooth Particle Hydrodynamics (SPH) - GADGET2, Springel 2005
- Gasoline, Wadsley, Stadel, & Quinn
Adaptive grid - ART+hydro - Klypin & Kravtsov
Moving Mesh - AREPO - Springel 2009

Initial Conditions

Standard: Gaussian P(k) realized uniformly, Zel'dovich displacement
Multimass - put lower mass particles in a small part of sim volume
Constrained realization - small scale: simulate individual halos (NFW)
- large scale: simulate particular region

Reviews

Bertschinger ARAA 1998, Klypin lectures 2002, Bagla 2004,
U Washington website

Latest Code for Hydrodynamical Simulations

Title: E pur si muove: Galilean-invariant cosmological hydrodynamical simulations on a moving mesh

Authors: Springel, Volker

Publication: eprint arXiv:0901.4107

Keywords: Astrophysics - Cosmology and Extra-Galactic Astrophysics

Comment: submitted to MNRAS, 66 pages, 50 figures, many of them heavily size-reduced. Full resolution version and videos available at http://www.mpa-garching.mpg.de/~volker/arepo

Abstract

Hydrodynamic cosmological simulations at present usually employ either the Lagrangian SPH technique, or Eulerian hydrodynamics on a Cartesian mesh with adaptive mesh refinement. Both of these methods have disadvantages that negatively impact their accuracy in certain situations. We here propose a novel scheme which largely eliminates these weaknesses. It is based on a moving unstructured mesh defined by the Voronoi tessellation of a set of discrete points. The mesh is used to solve the hyperbolic conservation laws of ideal hydrodynamics with a finite volume approach, based on a second-order unsplit Godunov scheme with an exact Riemann solver. The mesh-generating points can in principle be moved arbitrarily. If they are chosen to be stationary, the scheme is equivalent to an ordinary Eulerian method with second order accuracy. If they instead move with the velocity of the local flow, one obtains a Lagrangian formulation of hydrodynamics that does not suffer from the mesh distortion limitations inherent in other mesh-based Lagrangian schemes. In this mode, our new method is fully Galilean-invariant, unlike ordinary Eulerian codes, a property that is of significant importance for cosmological simulations. In addition, the new scheme can adjust its spatial resolution automatically and continuously, and hence inherits the principal advantage of SPH for simulations of cosmological structure growth. The high accuracy of Eulerian methods in the treatment of shocks is retained, while the treatment of contact discontinuities improves. We discuss how this approach is implemented in our new parallel code AREPO, both in 2D and 3D. We use a suite of test problems to examine the performance of the new code and argue that it provides an attractive and competitive alternative to current SPH and Eulerian techniques. (abridged)

AREPO Gas Disk Shearing

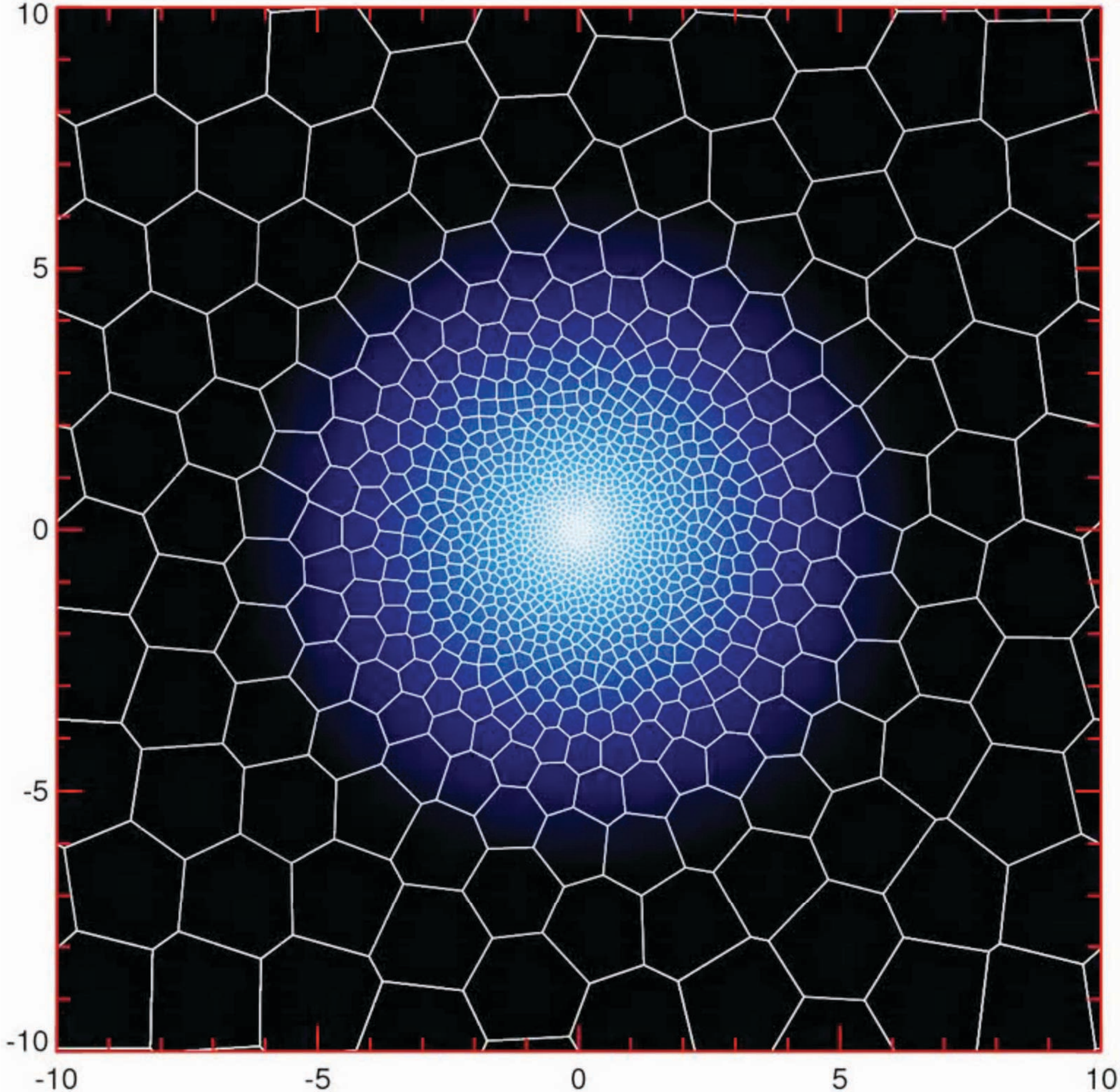

Structure of Dark Matter Halos

Navarro, Frenk, White

1996 1997 ⟶

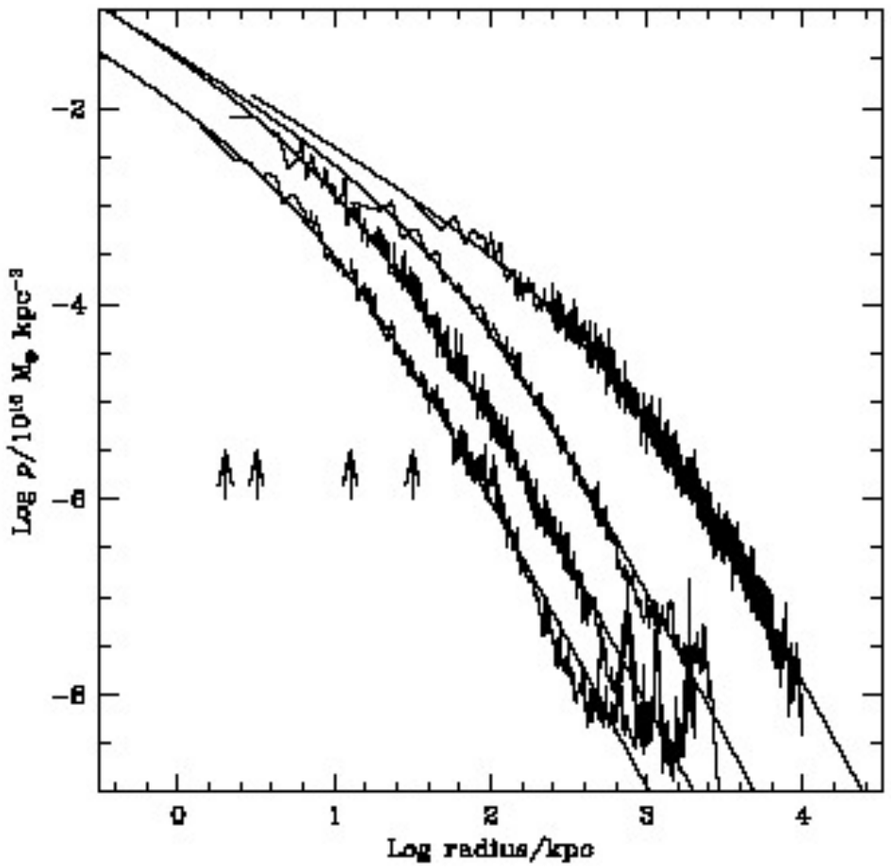

Fig. 3.— Density profiles of four halos spanning four orders of magnitude in mass. The arrows indicate the gravitational softening, h_g, of each simulation. Also shown are fits from eq.3. The fits are good over two decades in radius, approximately from h_g out to the virial radius of each system.

$$\frac{\rho(r)}{\rho_{crit}} = \frac{\delta_c}{(r/r_s)(1+r/r_s)^2}, \qquad (3)$$

NFW formula works for all models

Density

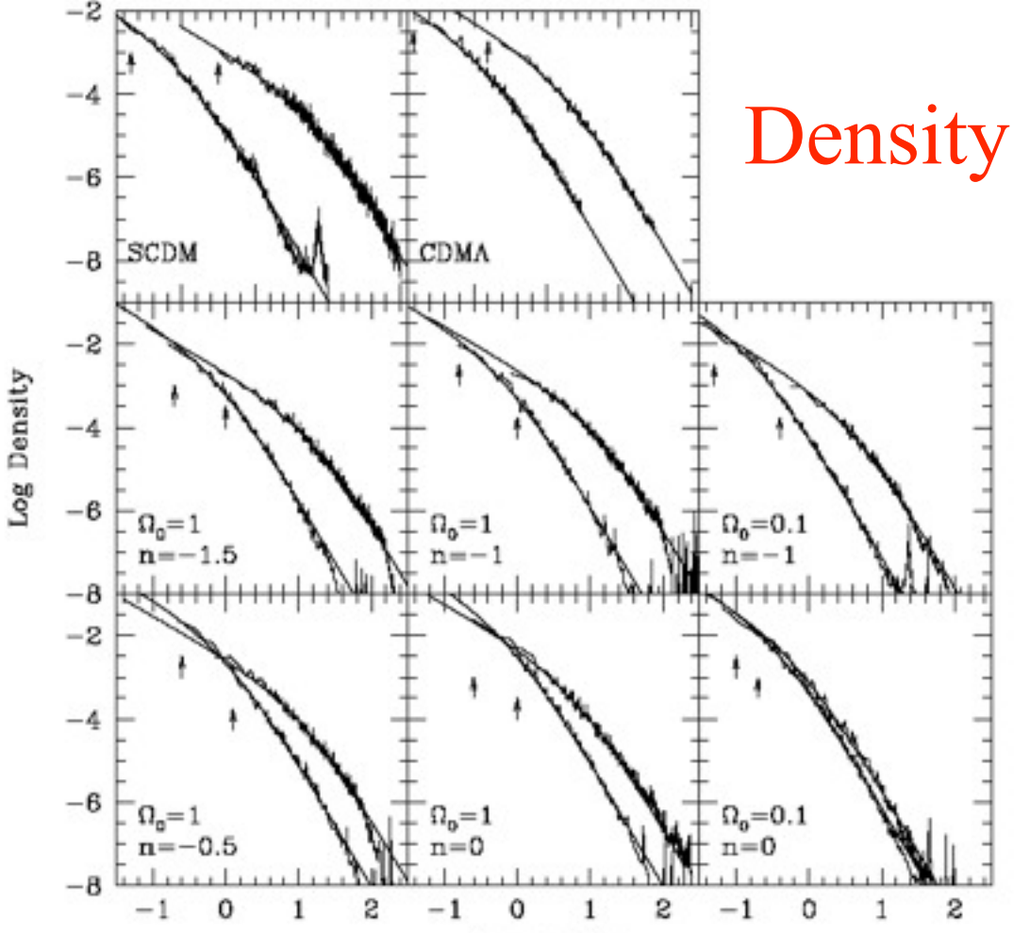

Velocity

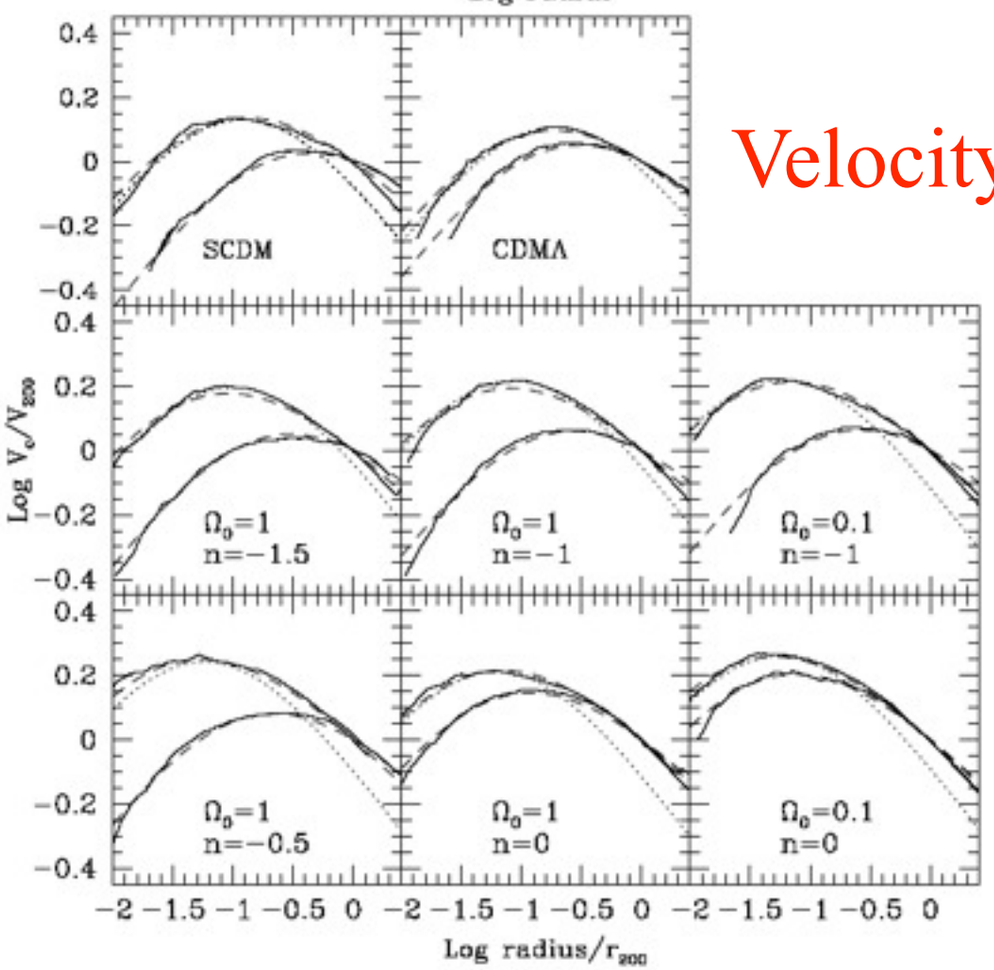

Part of James Bullock's dissertation research with Joel Primack

Dependence of Halo Concentration on Mass and Redshift

Profiles of dark haloes: evolution, scatter, and environment

J. S. Bullock[1,2], T. S. Kolatt[1,3], Y. Sigad[3], R.S. Somerville[3,4], A. V. Kravtsov[2,5⋆], A. A. Klypin[5], J. R. Primack[1], and A. Dekel[3] 2001 MNRAS 321, 559

ABSTRACT

We study dark-matter halo density profiles in a high-resolution N-body simulation of a ΛCDM cosmology. Our statistical sample contains ∼5000 haloes in the range $10^{11} - 10^{14} h^{-1} M_{\odot}$ and the resolution allows a study of subhaloes inside host haloes. The profiles are parameterized by an NFW form with two parameters, an inner radius r_s and a virial radius R_{vir}, and we define the halo concentration $c_{vir} \equiv R_{vir}/r_s$. We find that, for a given halo mass, the redshift dependence of the median concentration is $c_{vir} \propto (1+z)^{-1}$. This corresponds to $r_s(z) \sim$ constant, and is contrary to earlier suspicions that c_{vir} does not vary much with redshift. The implications are that high-redshift galaxies are predicted to be more extended and dimmer than expected before. Second, we find that the scatter in halo profiles is large, with a 1σ $\Delta(\log c_{vir}) = 0.18$ at a given mass, corresponding to a scatter in maximum rotation velocities of $\Delta V_{max}/V_{max} = 0.12$. We discuss implications for modelling the Tully-Fisher relation, which has a smaller reported intrinsic scatter. Third, subhaloes and haloes in dense environments tend to be more concentrated than isolated haloes, and show a larger scatter. These results suggest that c_{vir} is an essential parameter for the theory of galaxy modelling, and we briefly discuss implications for the universality of the Tully-Fisher relation, the formation of low surface brightness galaxies, and the origin of the Hubble sequence. We present an improved analytic treatment of halo formation that fits the measured relations between halo parameters and their redshift dependence, and can thus serve semi-analytic studies of galaxy formation.

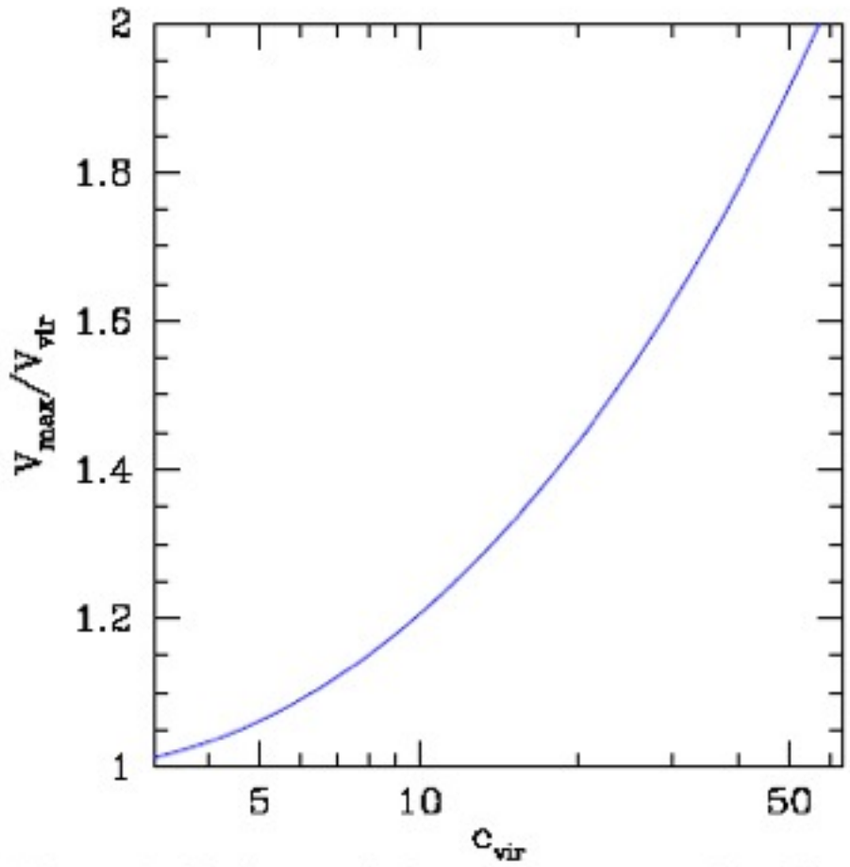

Figure 1. Maximum velocity versus concentration. The maximum rotation velocity for an NFW halo in units of the rotation velocity at its virial radius as a function of halo concentration.

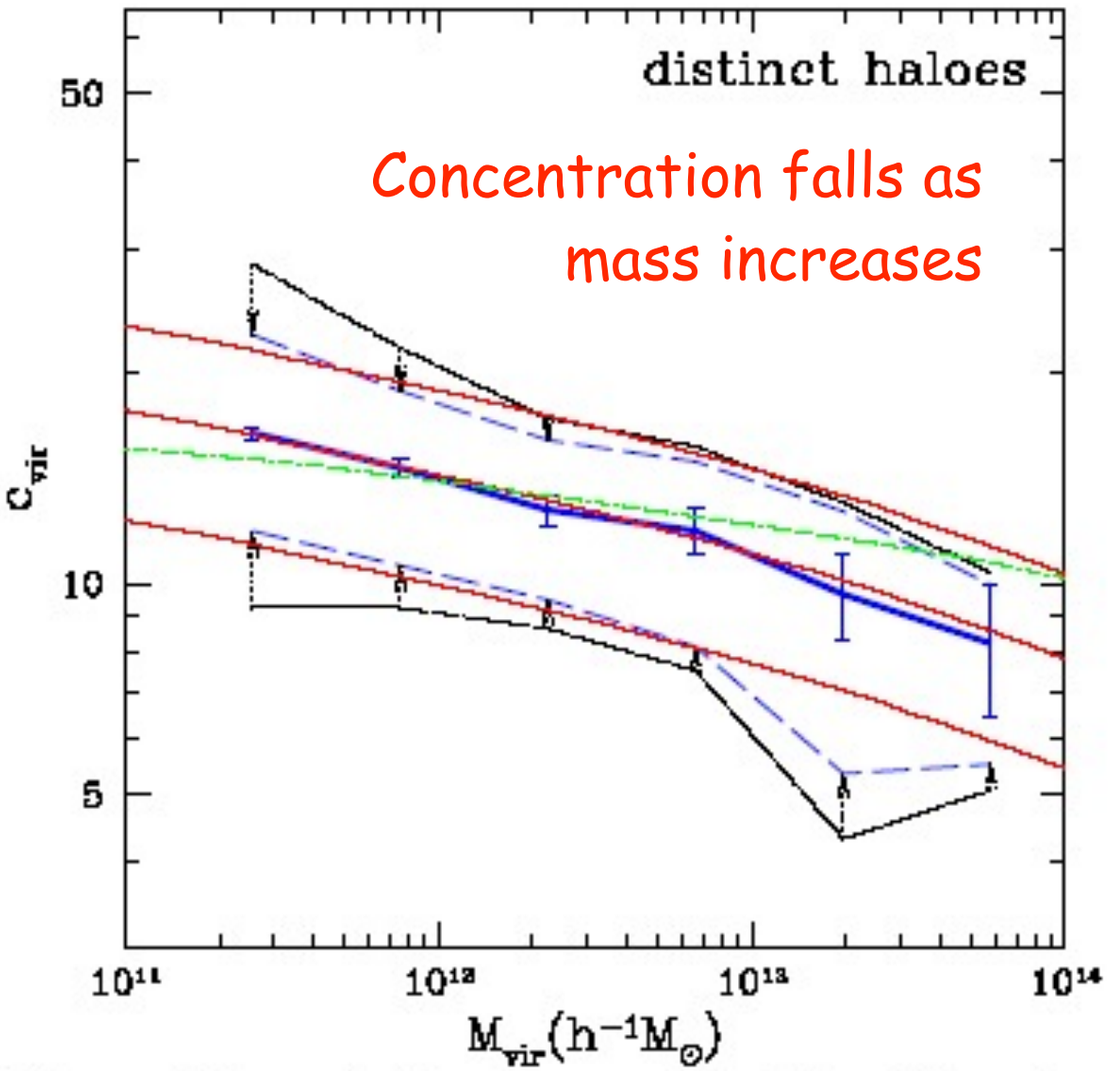

Figure 4. Concentration versus mass for distinct haloes at $z = 0$. The thick solid curve is the median at a given $M_{\rm vir}$. The error bars represent Poisson errors of the mean due to the sampling of a finite number of haloes per mass bin. The outer dot-dashed curves encompass 68% of the $c_{\rm vir}$ values as measured in the simulations. The inner dashed curves represent only the true, intrinsic scatter in $c_{\rm vir}$, after eliminating both the Poisson scatter and the scatter due to errors in the individual profile fits due, for example, to the finite number of particles per halo. The central and outer thin solid curves are the predictions for the median and 68% values by the toy model outlined in the text, for $F = 0.01$ and three different values of K. The thin dot-dashed line shows the prediction of the toy model of NFW97 for $f = 0.01$ and $k = 3.4 \times 10^3$.

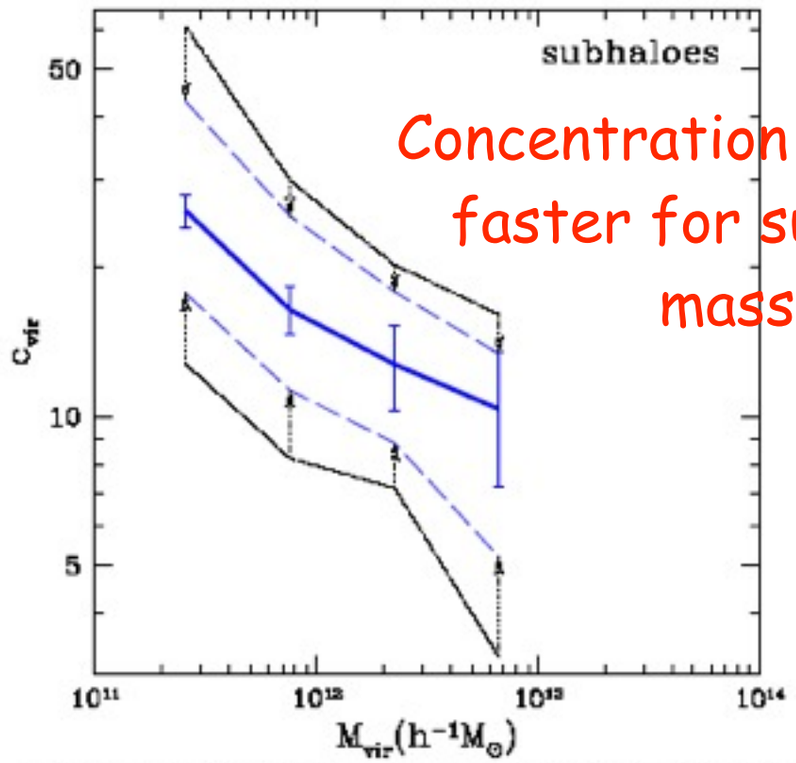

Figure 5. Concentration versus mass for subhaloes at $z = 0$. The curves and errors are the same as in Figure 4.

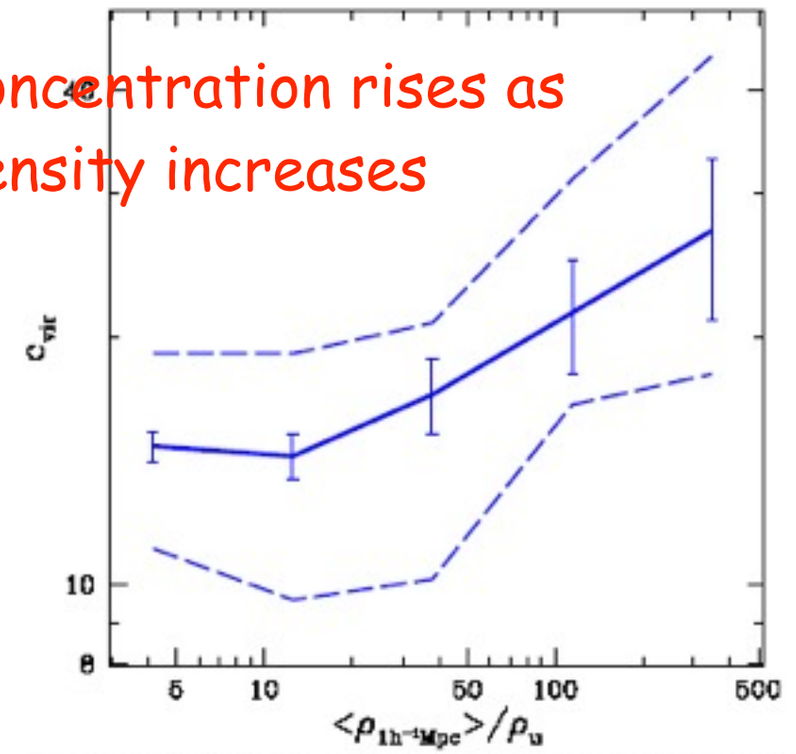

Figure 6. Concentrations versus environment. The concentration at $z = 0$ of all haloes in the mass range $0.5 - 1.0 \times 10^{12} h^{-1} M_\odot$ as a function of local density in units of the average density of the universe. The local density was determined within spheres of radius $1h^{-1}$Mpc. The solid line represents the median $c_{\rm vir}$ value, the error bars are Poisson based on the number of haloes, and the dashed line indicates our best estimate of the intrinsic scatter.

Spread of Halo Concentrations

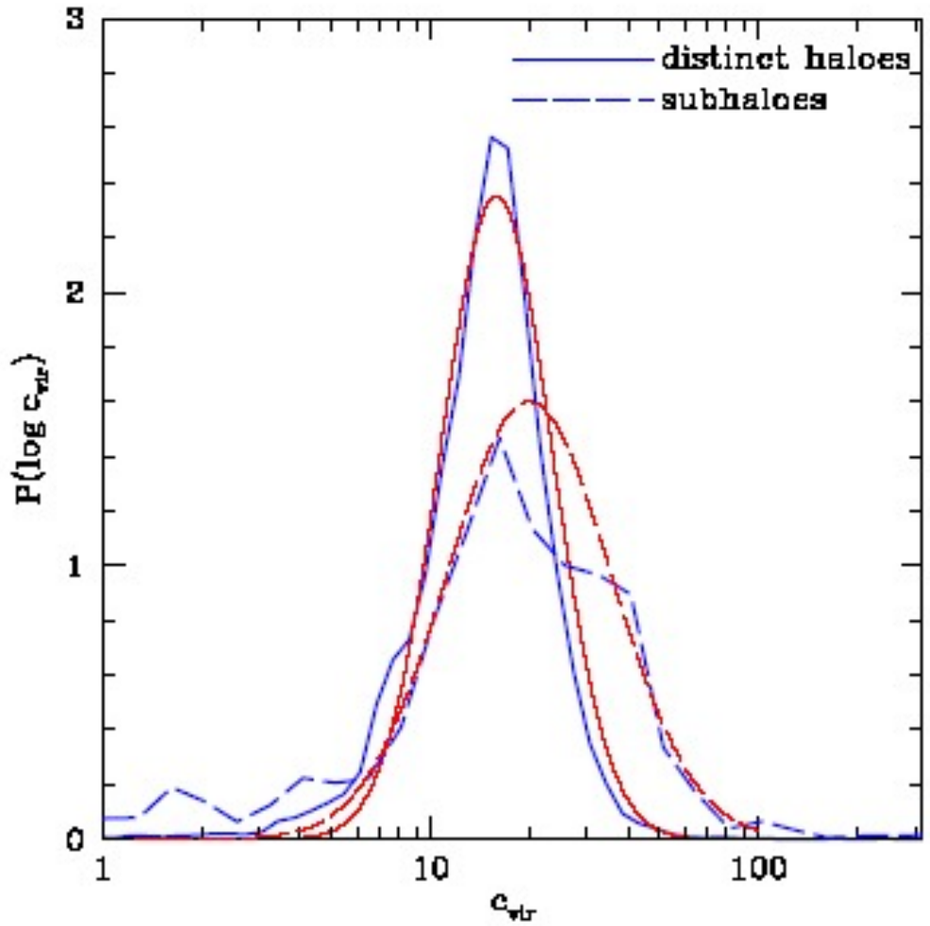

Figure 7. The probability distributions of distinct haloes (solid line) and subhaloes (dashed line) at $z = 0$ within the mass range $(0.5 - 1.0) \times 10^{12} h^{-1} M_{\odot}$. The simulated distributions (thick lines) include, the $\sim 2,000$ distinct haloes and ~ 200 subhaloes within this mass range. Log-normal distributions with the same median and standard deviation as the measured distributions are shown (thin lines). Subhaloes are, on average, more concentrated than distinct haloes and they show a larger spread.

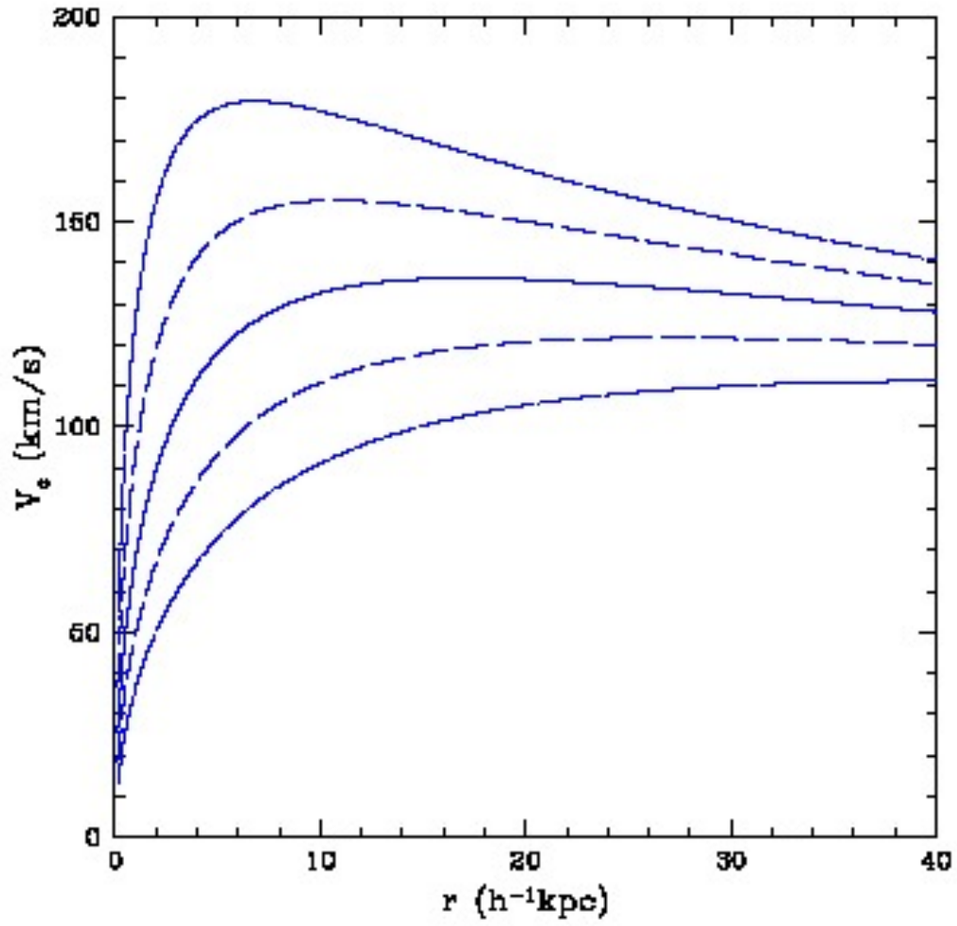

Figure 8. The spread in NFW rotation curves corresponding to the spread in concentration parameters for distinct haloes of $3 \times 10^{11} h^{-1} M_{\odot}$ at $z = 0$. Shown are the median (solid), $\pm 1\sigma$ (long dashed), and $\pm 2\sigma$ (dot-dashed) curves. The corresponding median rotation curve for subhaloes is comparable to the upper 1σ curve of distinct haloes.

Evolution of Halo Concentration with Redshift

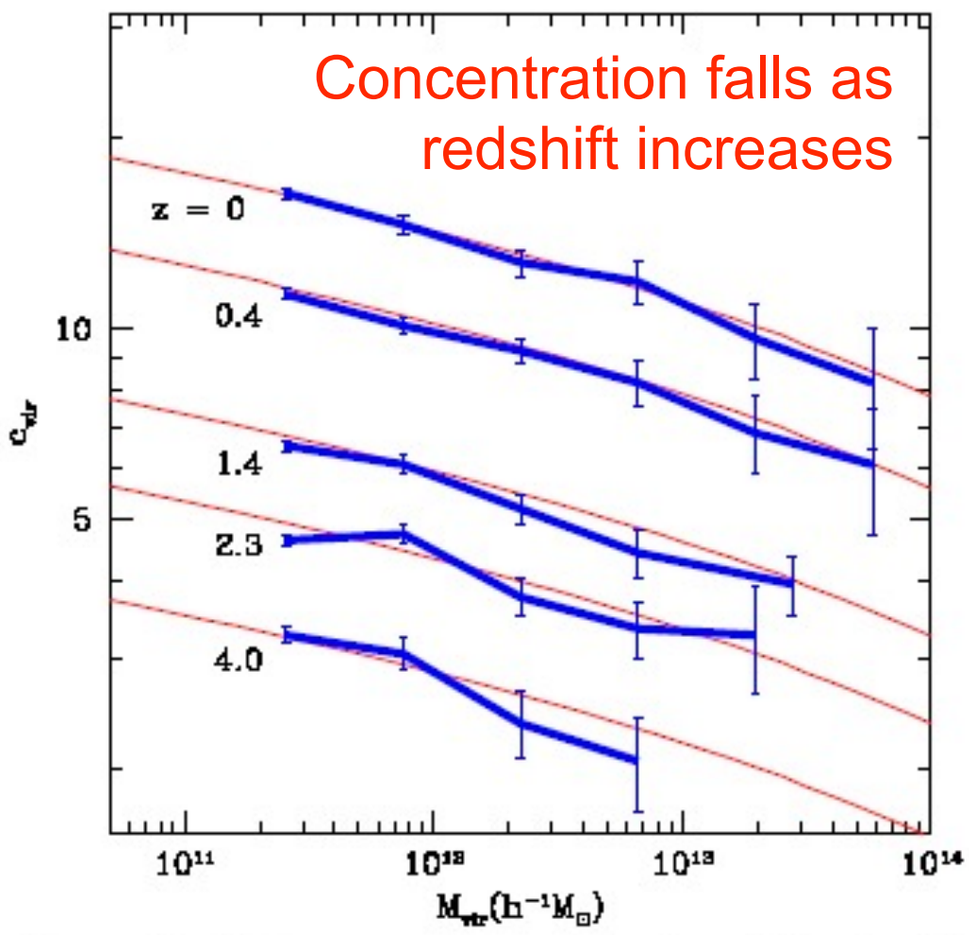

Figure 10. Median $c_{\rm vir}$ values as a function of $M_{\rm vir}$ for distinct haloes at various redshifts. The error bars are the Poisson errors due to the finite number of haloes in each mass bin. The thin solid lines show our toy model predictions.

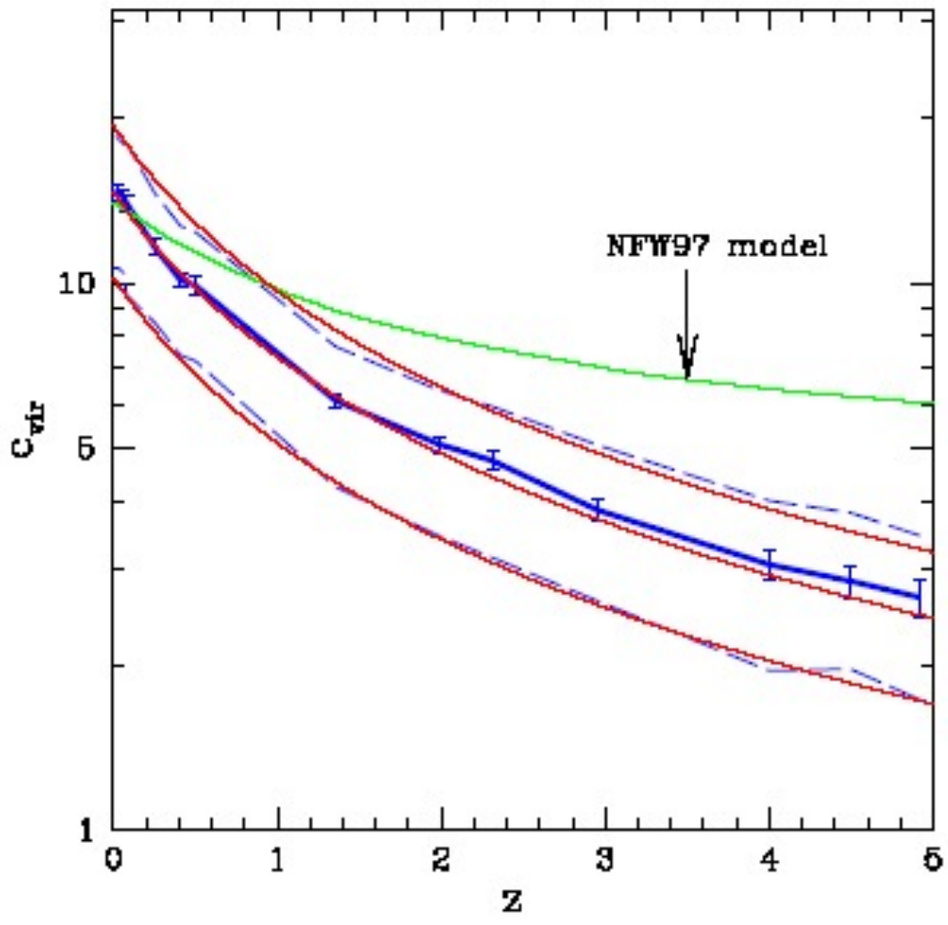

Figure 11. Concentration as a function of redshift for distinct haloes of a fixed mass, $M_{\rm vir} = 0.5 - 1.0 \times 10^{12} h^{-1} M_\odot$. The median (heavy solid line) and intrinsic 68% spread (dashed line) are shown. The behavior predicted by the NFW97 toy model is marked. Our revised toy model for the median and spread for $8 \times 10^{11} h^{-1} M_\odot$ haloes (thin solid lines) reproduces the observed behavior rather well.

$C_{vir} \propto 1/(1+z)$
at fixed mass

Merger Trees

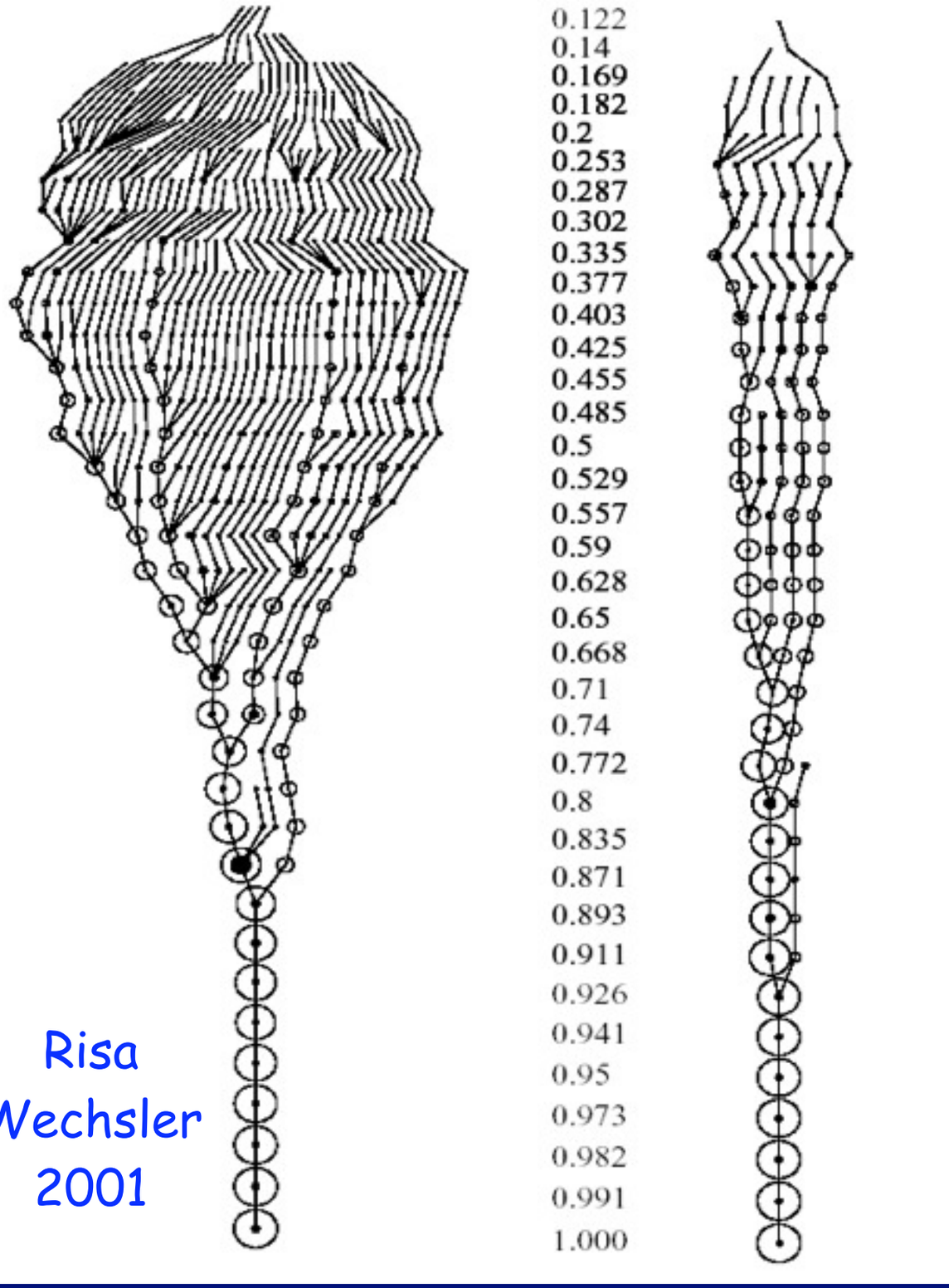

Risa Wechsler 2001

Based on our ART simulations, Wechsler created the first structural merger trees tracing the merging history of thousands of halos with structural information on their higher-redshift progenitors, including their radial profiles and spins. This led to the discovery that a halo's merging history can be characterized by a single parameter a_c which describes the scale factor at which the halo's mass accretion slows, and that this parameter correlates very well with the halo concentration, thus showing that the distribution of dark matter halo concentrations reflects mostly the distribution of their mass accretion rates. We found that the radius of the inner part of the halo, where the density profile is roughly 1/r, is established during the early, rapid-accretion phase of halo growth (a result subsequently confirmed and extended by other groups, e.g., Zhao et al. 2003, Reed et al. 2004).

Evolution of Halo Maximum Circular Velocity

Bullock, Dekel, Kolatt, Primack, & Somerville 2001, ApJ, 550, 21

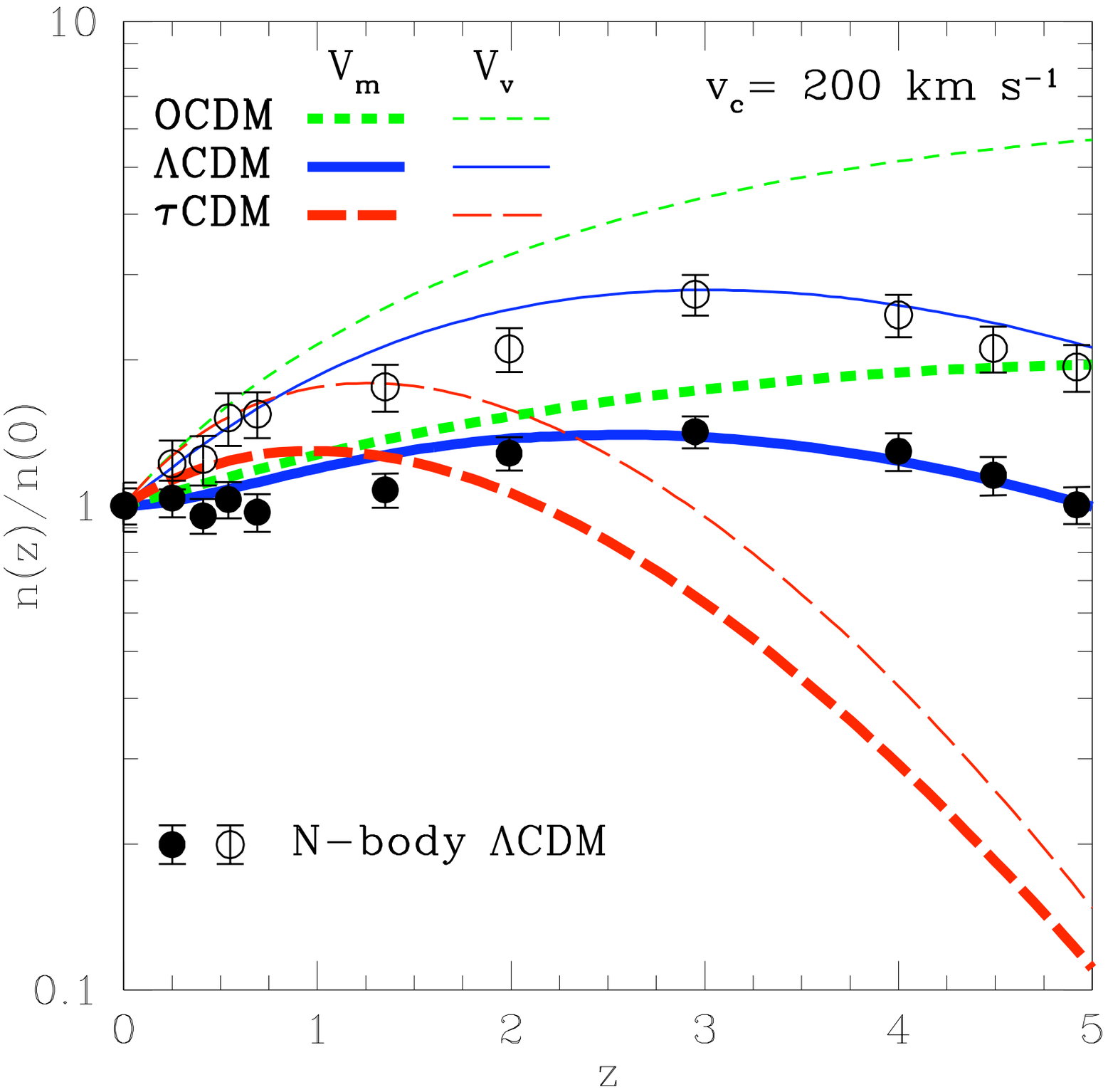

FIG. 1.— Evolution of relative comoving number density for fixed $v_{\rm m} = 200\,{\rm km\,s^{-1}}$ (bold curves) and $v_{\rm v} = 200\,{\rm km\,s^{-1}}$ halos in three cosmologies.

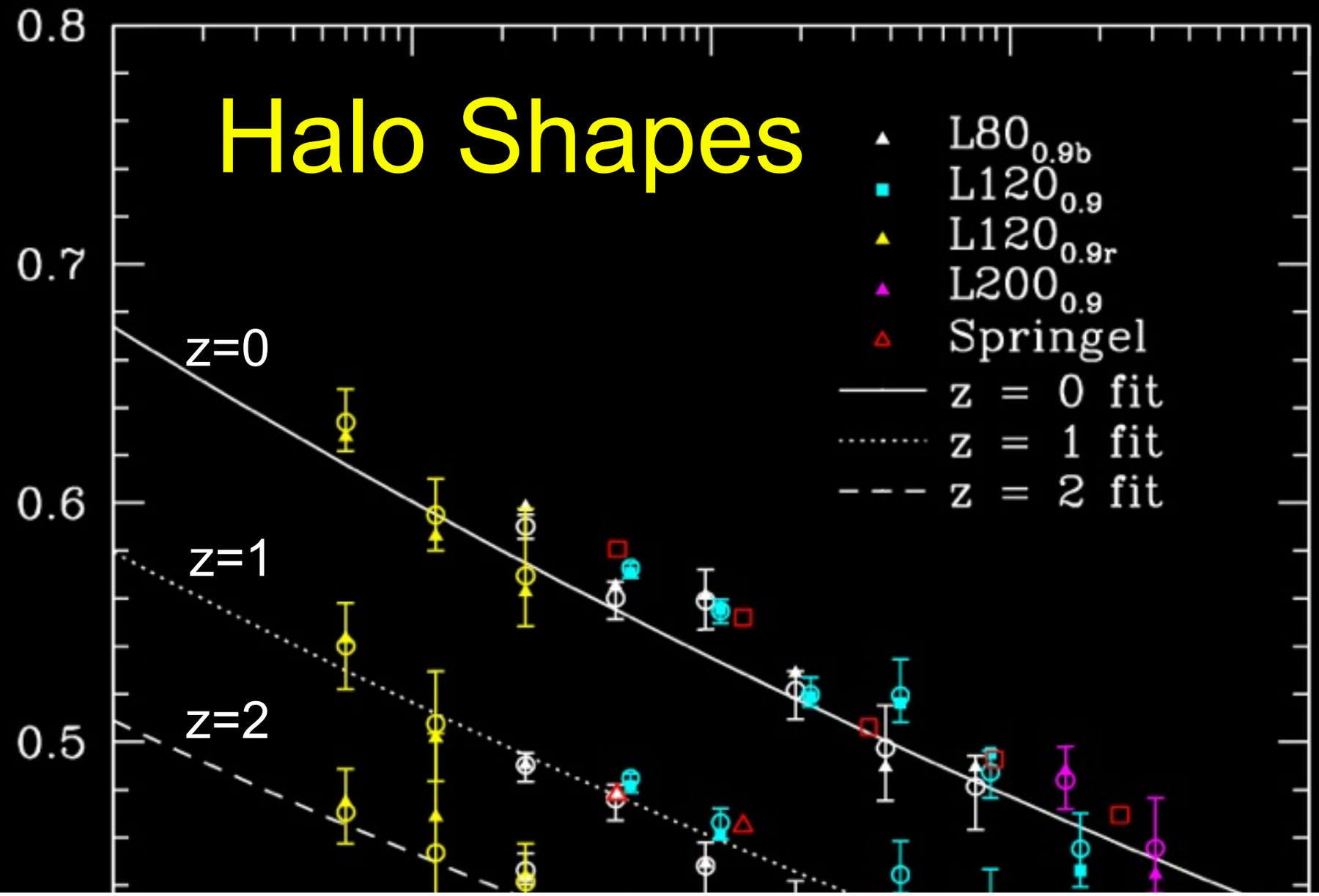

A simple formula describes these results, as well dependence on epoch and cosmological parameter σ_8 :

$$\langle s \rangle (M_{\rm vir}, z = 0) = \alpha \left(\frac{M_{\rm vir}}{M_*} \right)^{\beta}$$

with best fit values

$$\alpha = 0.54 \pm 0.03, \ \beta = -0.050 \pm 0.003.$$

<s> = short / long axis of dark halos vs. mass and redshift. Dark halos are more elongated the more massive they are and the earlier they form. We found that the halo <s> scales as a power-law in Mhalo/M*. Halo shape is also related to the Wechsler halo formation scale factor a_c.

Allgood et al. 2006

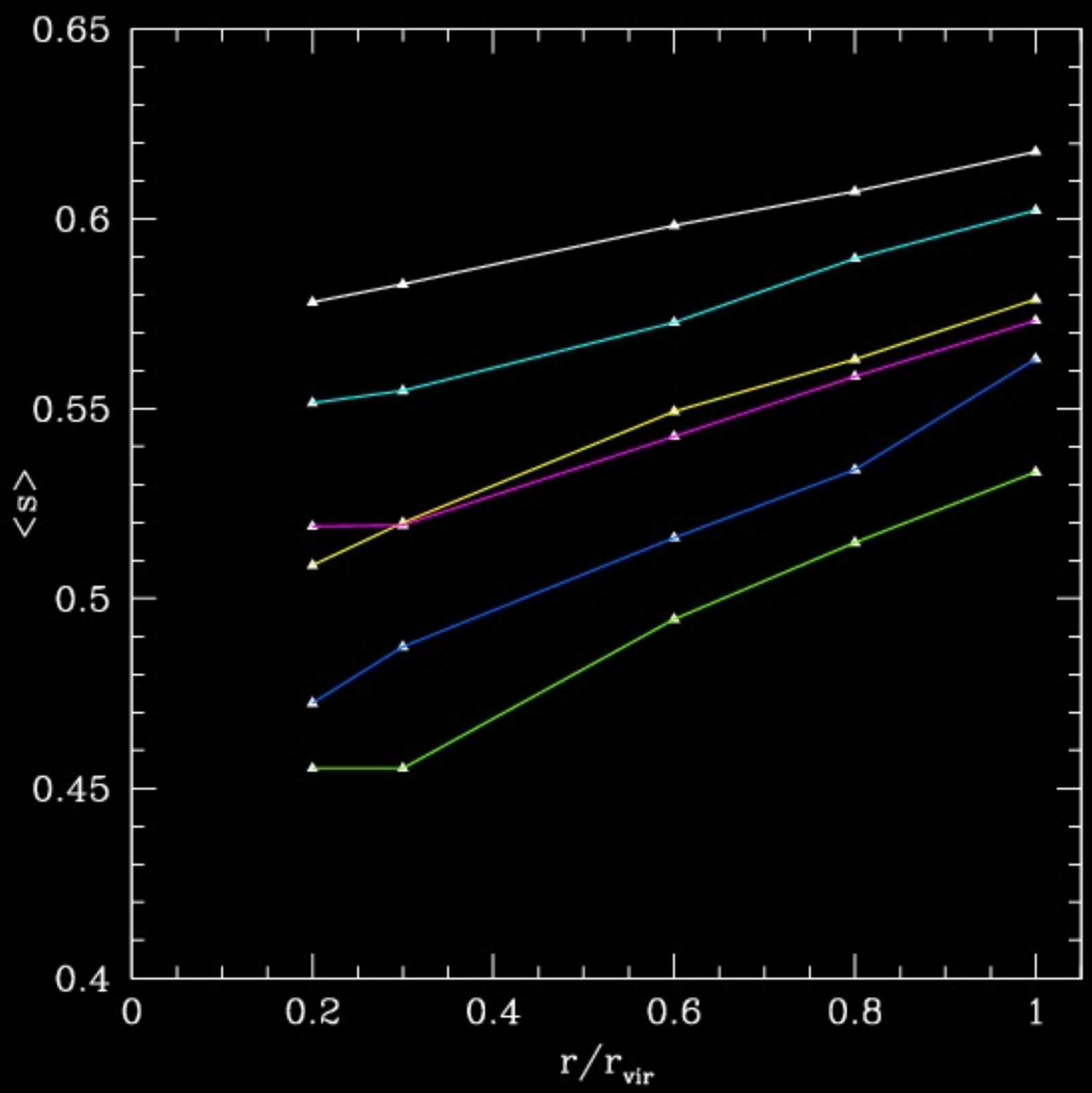

FIG. 7.— $\langle s \rangle$ with radius at $z = 0$. black: $1.6 \times 10^{12} < M < 3.2 \times 10^{12}$, red: $3.2 \times 10^{12} < M < 6.4 \times 10^{12}$, blue: $6.4 \times 10^{12} < M < 1.28 \times 10^{13}$, green: $1.28 \times 10^{13} < M < 2.56 \times 10^{13}$, orange: $2.56 \times 10^{13} < M < 5.12 \times 10^{13}$, violet: $5.12 \times 10^{13} < M$. These are the same mass bins as in Figure 3.

Halos become more spherical at larger radius and smaller mass.
As before,
s = short / long axis. These predictions can be tested against cluster X-ray data and galaxy weak lensing data.

[These figures are from Brandon Allgood's PhD dissertation.]

Multimass Simulation of Halos

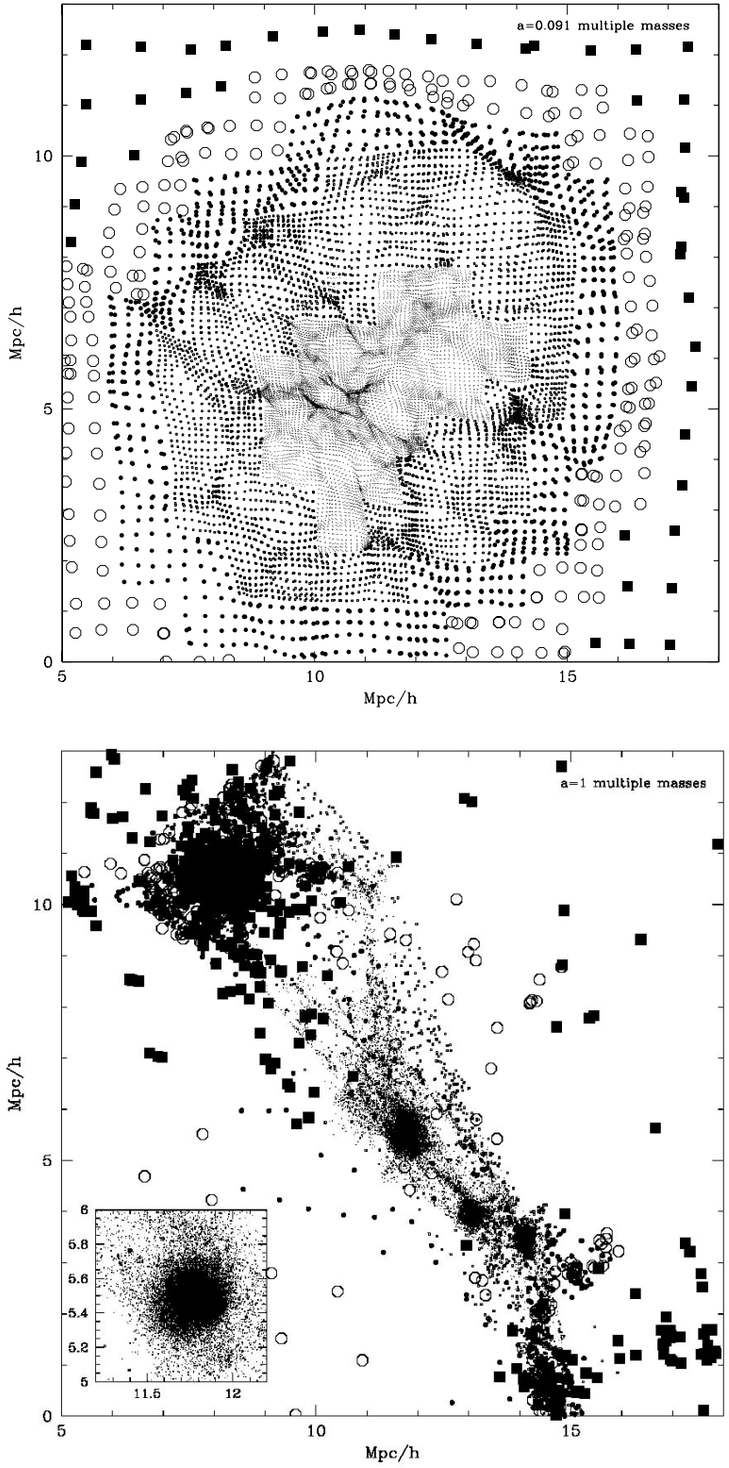

Fig. 2.— Distribution of particles of different masses in a thin slice through the center of halo A_1 (see Table 1) at $z = 10$ (top panel) and at $z = 0$ (bottom panel). To avoid crowding of points the thickness of the slice is made smaller in the center (about $30h^{-1}$kpc) and larger ($1h^{-1}$Mpc) in the outer parts of the forming halo. Particles of different mass are shown with different symbols: tiny dots, dots, large dots, squares, and open circles.

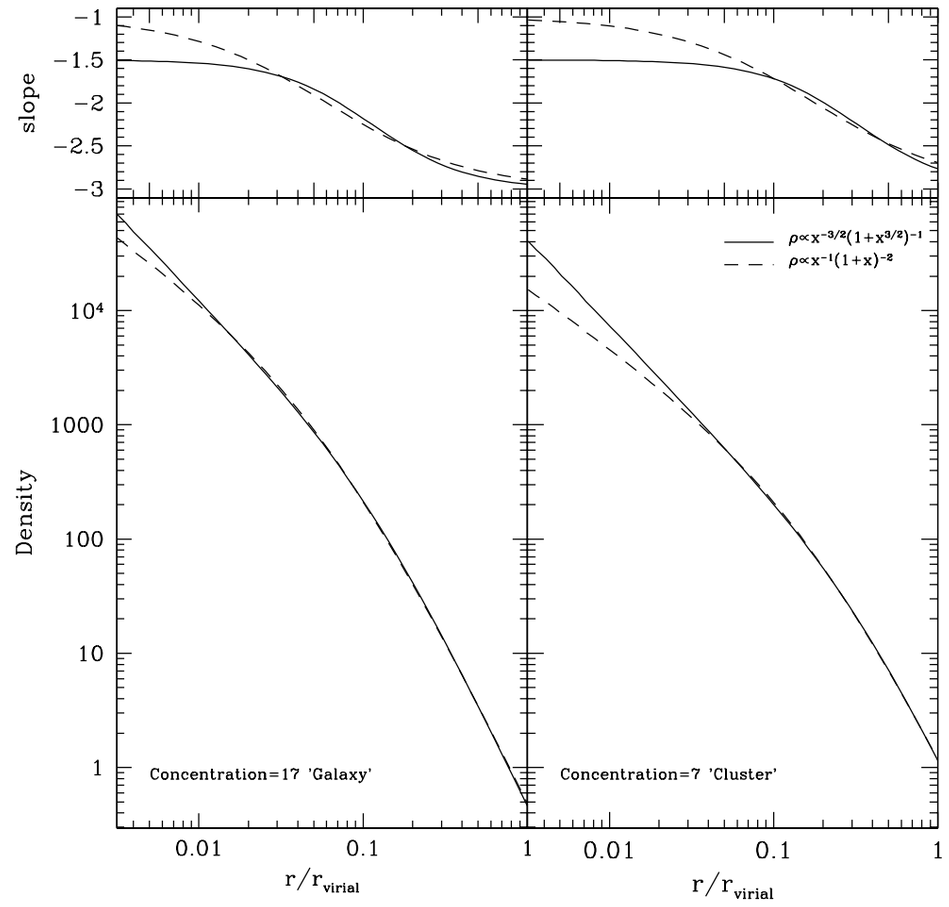

Fig. 3.— Comparison of the Moore et al. and the NFW profiles. Each profile is normalized to have the same virial mass and the same radius of the maximum circular velocity. *Left panels:* High-concentration halo typical of small galaxy-size halos $C_{\rm NFW} = 17$. *Right panels:* Low-concentration halo typical of cluster-size halos. The deviations are very small ($< 3\%$) for radii $r > r_s/2$. Top panels show the local logarithmic slope of the profiles. Note that for the high concentration halo the slope of the profile is significantly larger than the asymptotic value -1 even at very small radii $r \approx 0.01 r_{\rm vir}$.

Klypin, Kravtsov, Bullock & Primack 2001

Dark Matter Halo Radial Profile

Comparison of NFW and Moore et al. profiles

Parameter	NFW	Moore et al.
Density $x = r/r_s$	$\rho = \frac{\rho_s}{x(1+x)^2}$ $\rho \propto x^{-3}$ for $x \gg 1$ $\rho \propto x^{-1}$ for $x \ll 1$ $\rho/\rho_s = 1/4$ at $x = 1$	$\rho = \frac{\rho_s}{x^{1.5}(1+x)^{1.5}}$ $\rho \propto x^{-3}$ for $x \gg 1$ $\rho \propto x^{-1.5}$ for $x \ll 1$ $\rho/\rho_s = 1/2$ at $x = 1$
Mass $M = 4\pi\rho_s r_s^3 f(x)$ $= M_{\rm vir} f(x)/f(C)$ $M_{\rm vir} = \frac{4\pi}{3}\rho_{\rm cr}\Omega_0\delta_{\rm top-hat} r_{\rm vir}^3$	$f(x) = \ln(1+x) - \frac{x}{1+x}$	$f(x) = \frac{2}{3}\ln(1+x^{3/2})$
Concentration $C = r_{\rm vir}/r_s$	$C_{\rm NFW} = 1.72 C_{\rm Moore}$ for halos with the same $M_{\rm vir}$ and $r_{\rm max}$ $C_{1/5} \approx \frac{C_{\rm NFW}}{0.86 f(C_{\rm NFW}) + 0.1363}$ error less than 3% for $C_{\rm NFW}$ =5-30 $C_{\gamma=-2} = C_{\rm NFW}$	$C_{\rm Moore} = C_{\rm NFW}/1.72$ $C_{1/5} = \frac{C_{\rm Moore}}{[(1+C_{\rm Moore}^{3/2})^{1/5} - 1]^{2/3}}$ $\approx \frac{C_{\rm Moore}}{[C_{\rm Moore}^{3/10} - 1]^{2/3}}$ $C_{\gamma=-2} = 2^{3/2} C_{\rm Moore}$ $\approx 2.83 C_{\rm Moore}$
Circular Velocity $v_{\rm circ}^2 = \frac{GM_{\rm vir}}{r_{\rm vir}}\frac{C}{x}\frac{f(x)}{f(C)}$ $= v_{\rm max}^2 \frac{x_{\rm max}}{x}\frac{f(x)}{f(x_{\rm max})}$ $v_{\rm vir}^2 = \frac{GM_{\rm vir}}{r_{\rm vir}}$	$x_{\rm max} \approx 2.15$ $v_{\rm max}^2 \approx 0.216 v_{\rm vir}^2 \frac{C}{f(C)}$ $\rho/\rho_s \approx 1/21.3$ at $x = 2.15$	$x_{\rm max} \approx 1.25$ $v_{\rm max}^2 \approx 0.466 v_{\rm vir}^2 \frac{C}{f(C)}$ $\rho/\rho_s \approx 1/3.35$ at $x = 1.25$

Klypin, Kravtsov, Bullock & Primack 2001

Empirical Models for Dark Matter Halos. II. Inner profile slopes, dynamical profiles, and ρ/σ^3

Alister Graham, David Merritt, Ben Moore, Jürg Diemand, Balša Terzić

2006, AJ 132, 2701

Einasto's model is given by the equation

$$\rho(r) = \rho_e \exp\left\{-d_n\left[(r/r_e)^{1/n} - 1\right]\right\}.$$

Data on log slopes from innermost resolved radius of observed galaxies, not corrected for observational effects -- adapted from de Blok (2004).

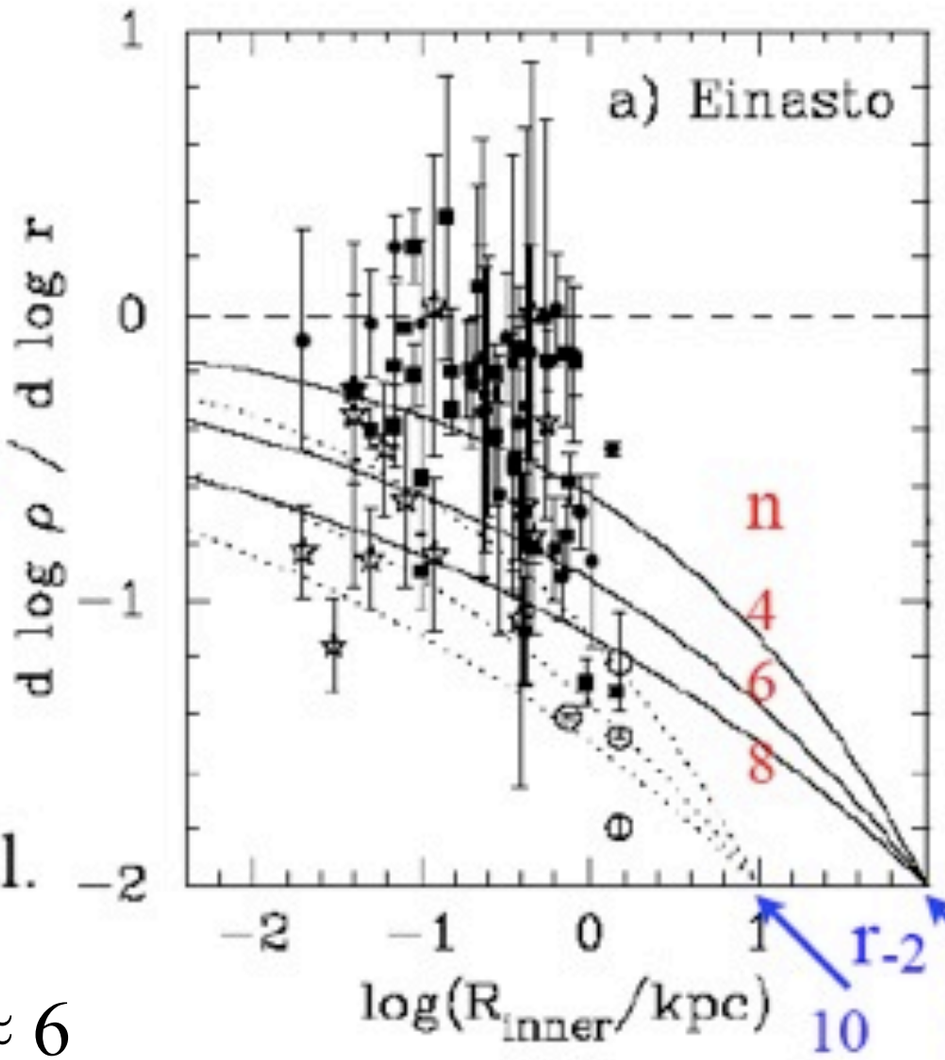

r_{-2} is the radius where the log-slope is -2

See also Navarro et al. Aquarius simulations arXiv:0810.1522: $n \approx 6$

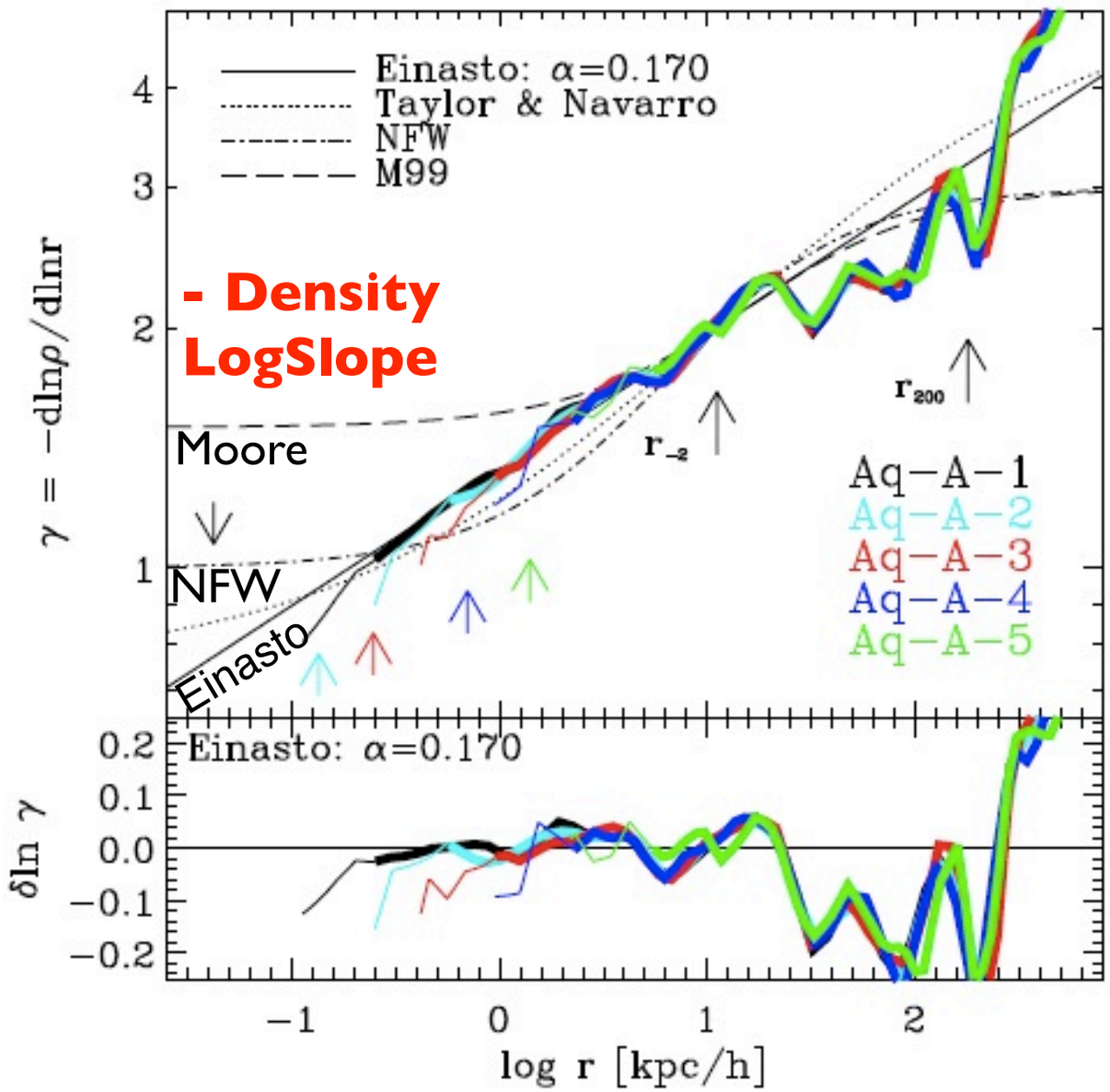

Logarithmic slope of the density profile as a function of radius for our Aq-A convergence series (using WMAP1 initial conditions). Thick lines show results for r > r(7) conv, thin lines extend the profiles down to the less strict convergence radius r(1) conv. Comparison shows that excellent numerical convergence for the slope is achieved down to a radius intermediate between these two convergence radii. Applied to the highest-resolution Aq-A-1 simulation (1.1×10^9 particles each of mass 10^3 $M_\odot$ within R_{vir}), this implies that the slope is shallower than the asymptotic value of the NFW profile (r−1) in the inner regions.We see no sign of convergence to an asymptotic inner power-law. Instead, the profiles get shallower toward the centre as predicted by the Einasto formula $\ln(\rho(r)/\rho_{-2}) = (-2/\alpha)[(r/r_{-2})^\alpha - 1]$ (a straight line in this plot). Arrows indicate the softening length h_s of each simulation.
Navarro et al. arXiv:0810.1522

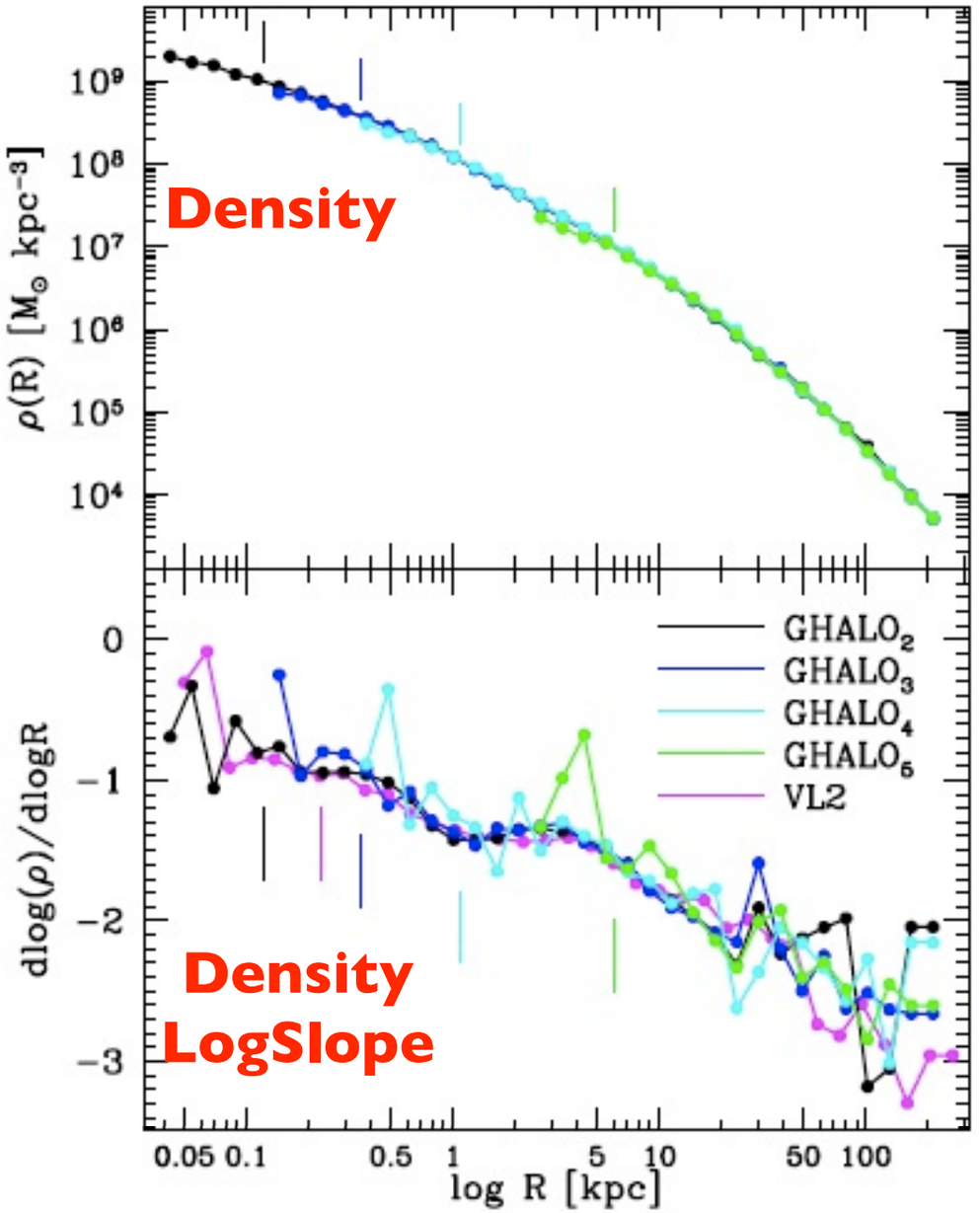

The density profile of GHALO2 (1.3×10^9 particles each of mass 10^3 $M_\odot$ within R_{200} = 347 kpc using WMAP3 initial conditions) and its lower resolution realizations as well as the density profile of the Via Lactea 2 simulation (mass 2×10^{12} $M_\odot$) in magenta. The convergence radius at each step in resolution is easily seen (indicated by the tick marks). Stadel et al. arXiv:0808.2981

The power law index $\gamma \approx 1$ at the smallest resolved radii, but it appears to decline further at smaller radii.

Aquarius: the Billennium simulation

The Aquarius "Billennium" halo simulation. A dark matter halo with 1 billion particles within the virial radius.

Volker Springel
Max Planck Institute for Astrophysics

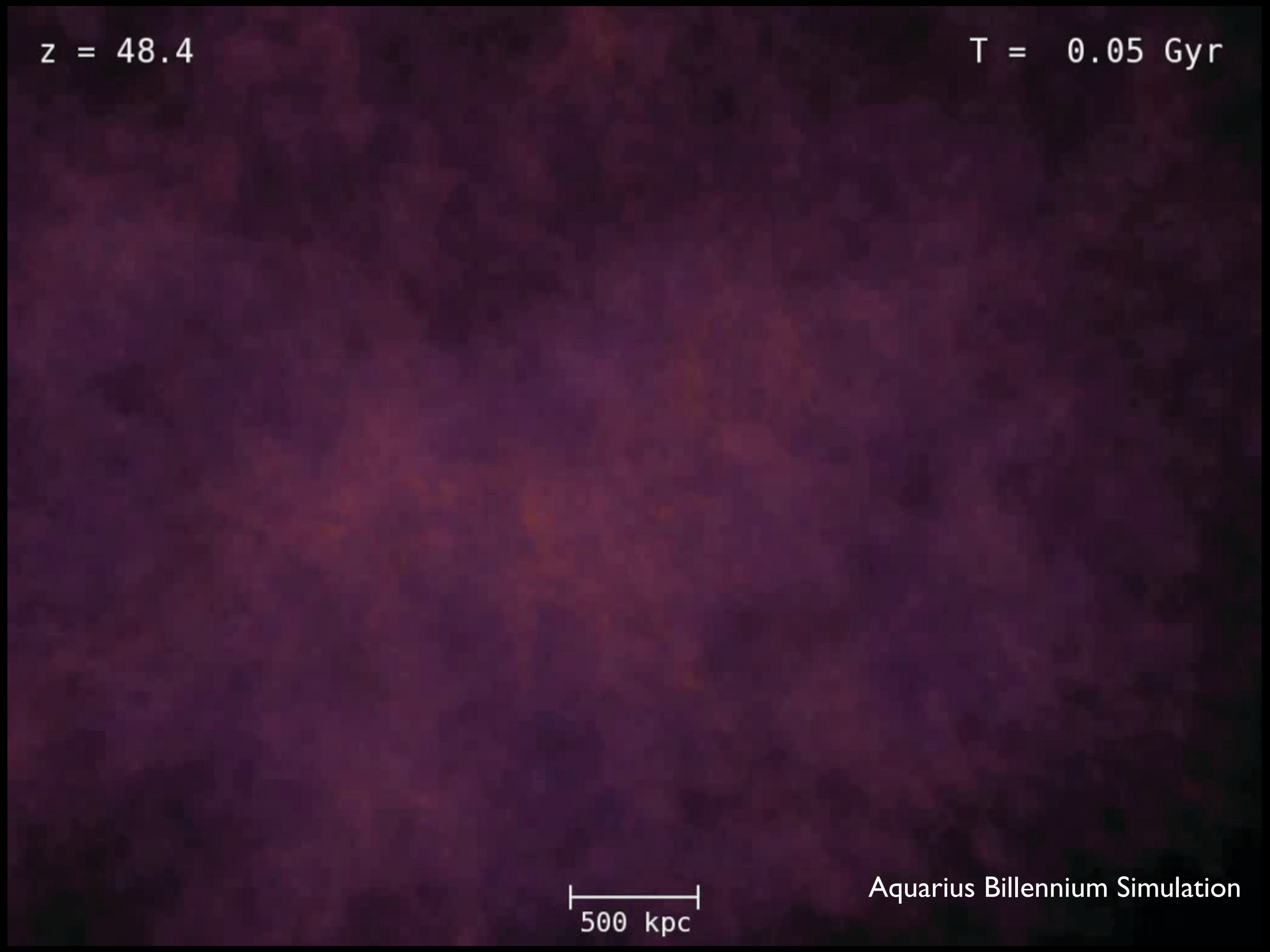
z = 48.4
T = 0.05 Gyr
500 kpc
Aquarius Billennium Simulation

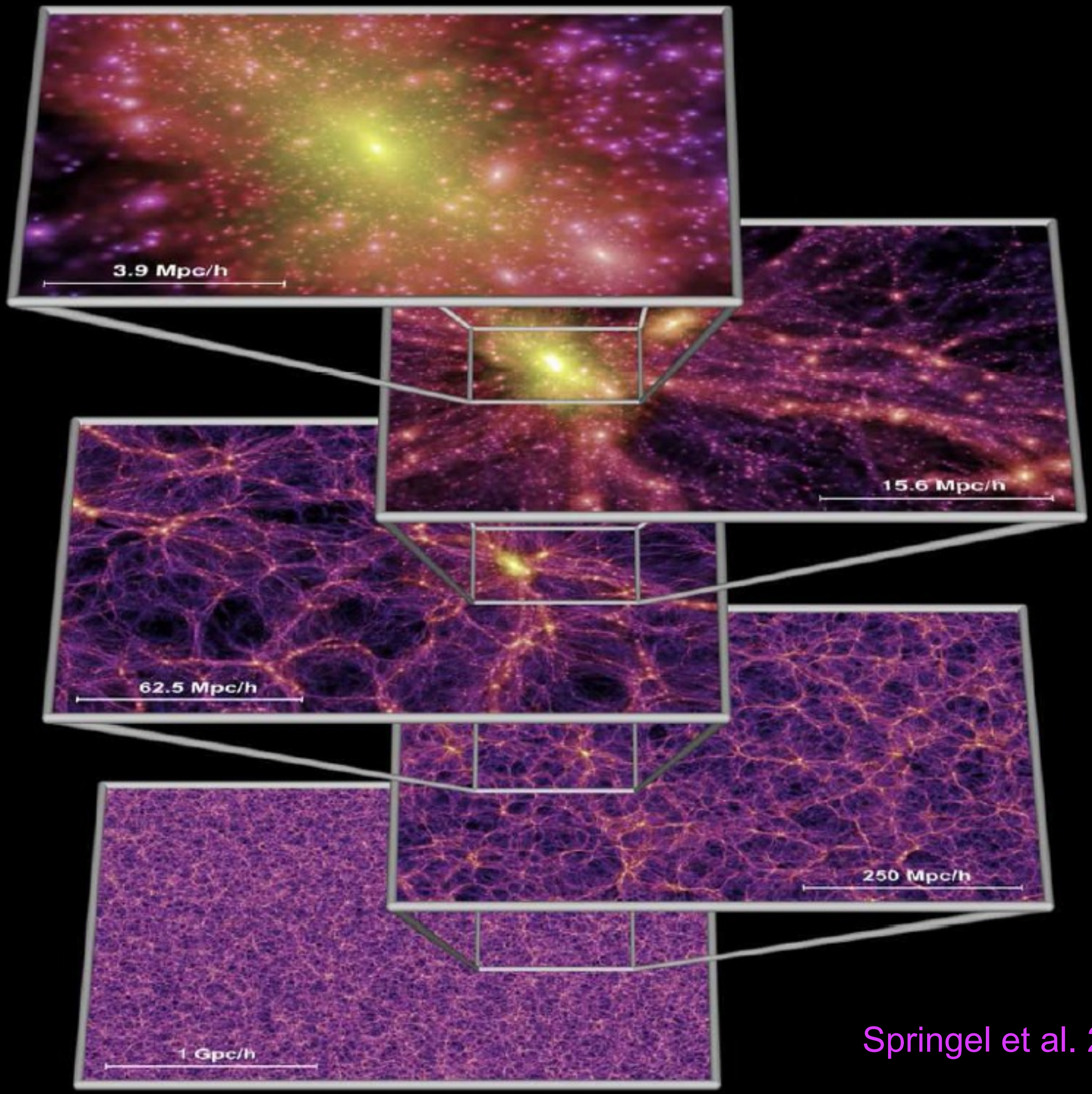

Springel et al. 2005

Particle number in cosmological N-body simulations vs. pub date

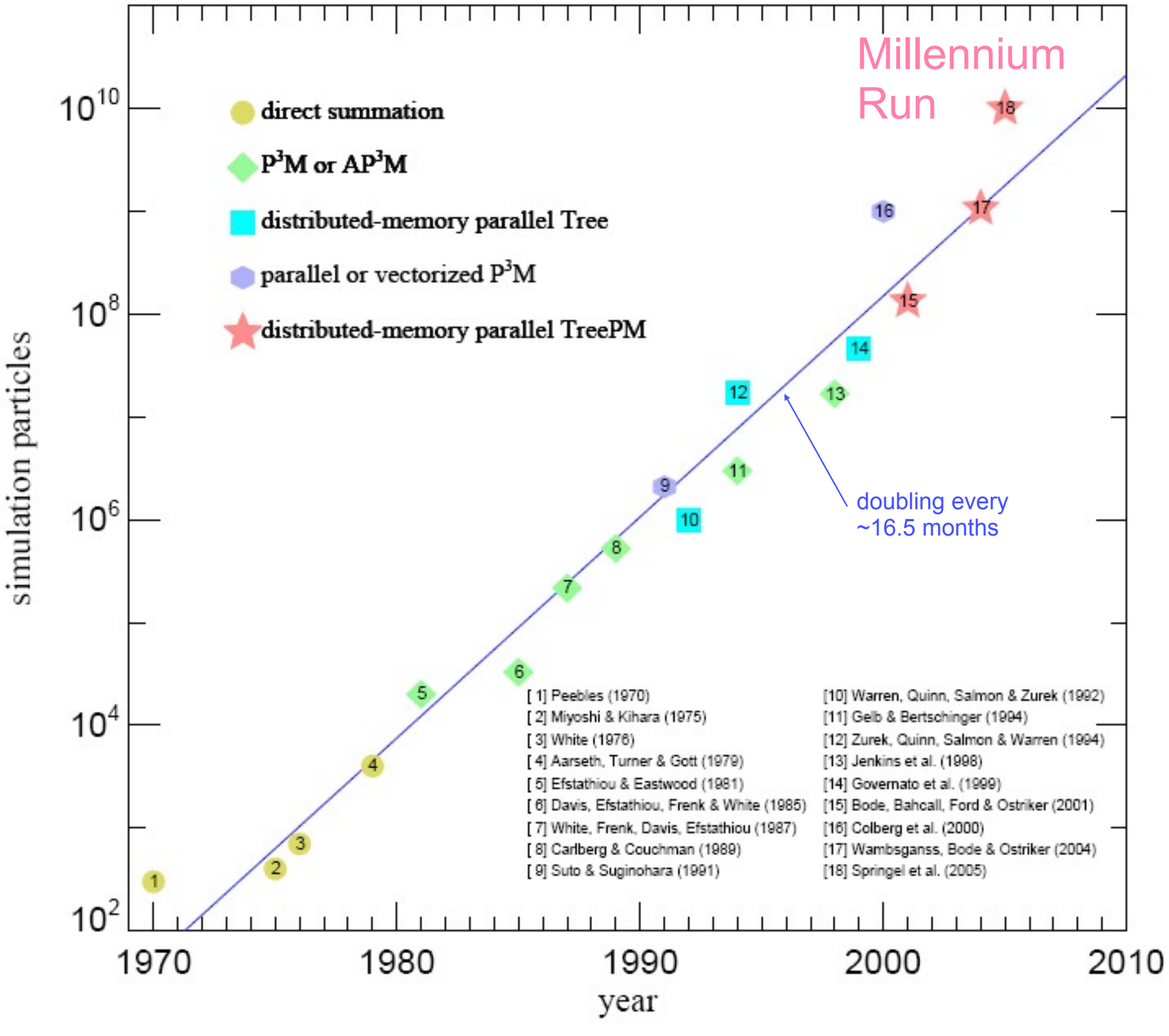

UNDERSTANDING GALAXY CORRELATIONS

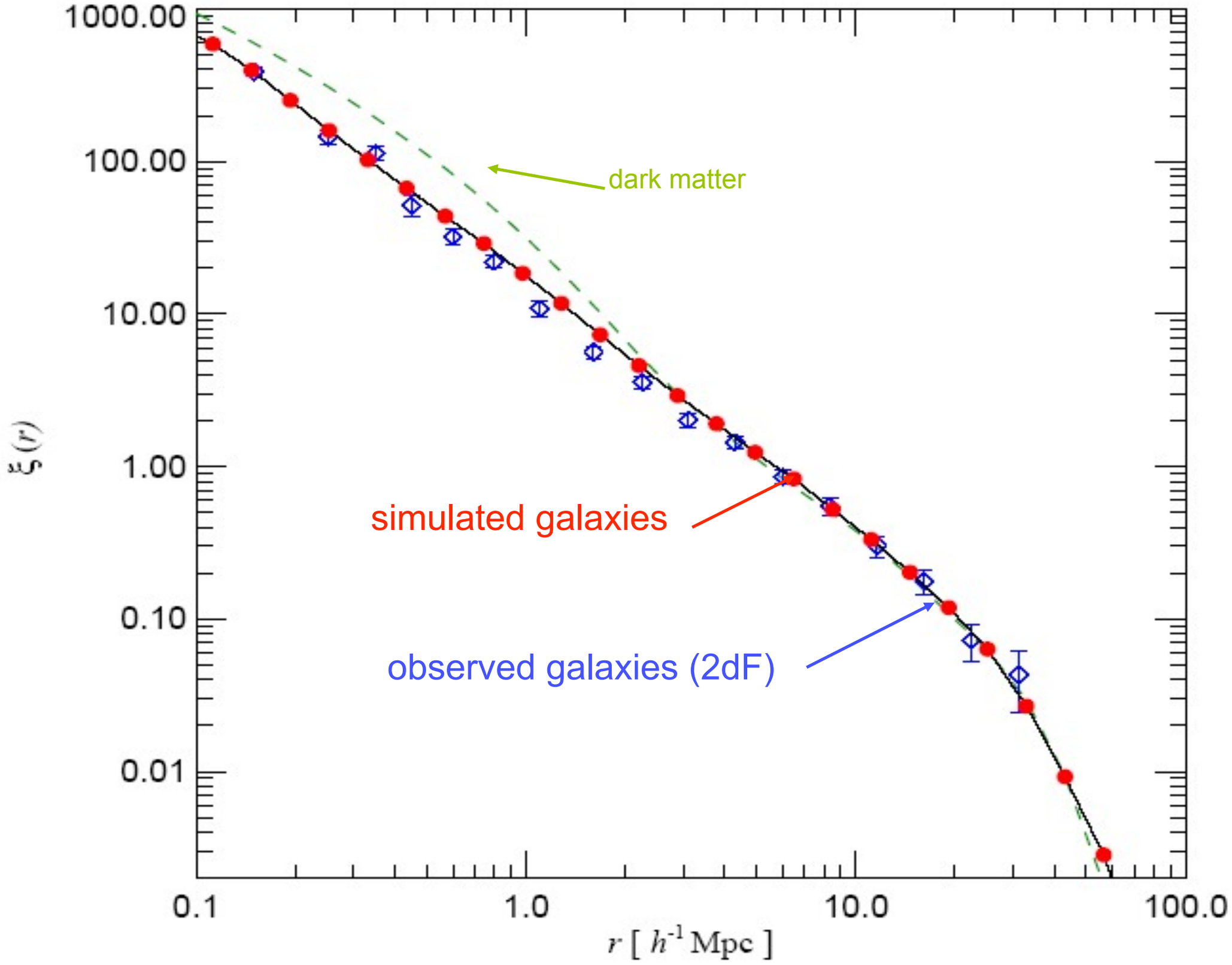

Galaxy 2-point correlation function at the present epoch.

Springel et al. 2005

Galaxy type correlated with large scale structure

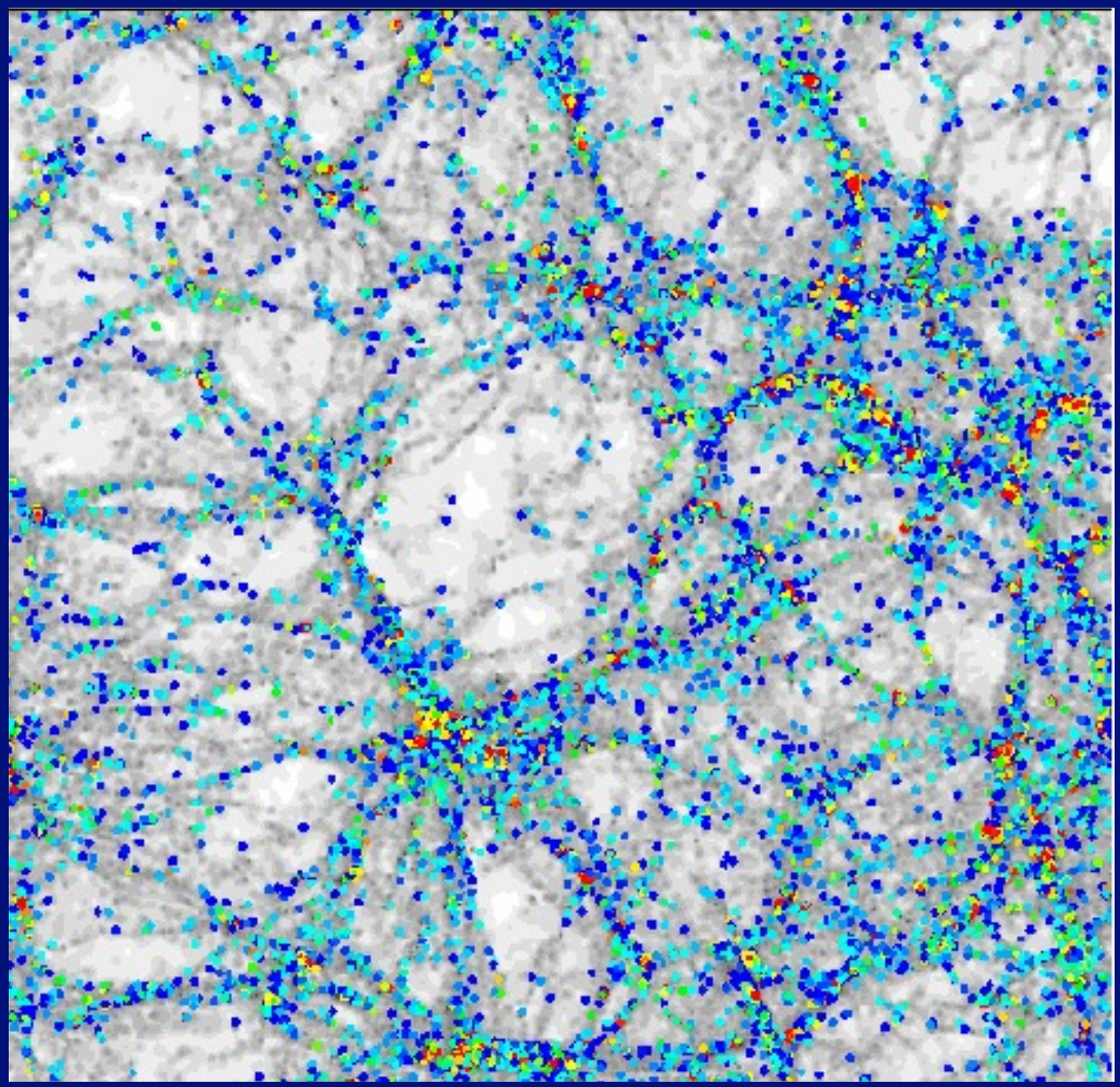

elliptical

elliptical

bulge+disk

disk

Semi-Analytic Modeling

Kauffmann et al.

Elliptical galaxies in clusters in the local universe

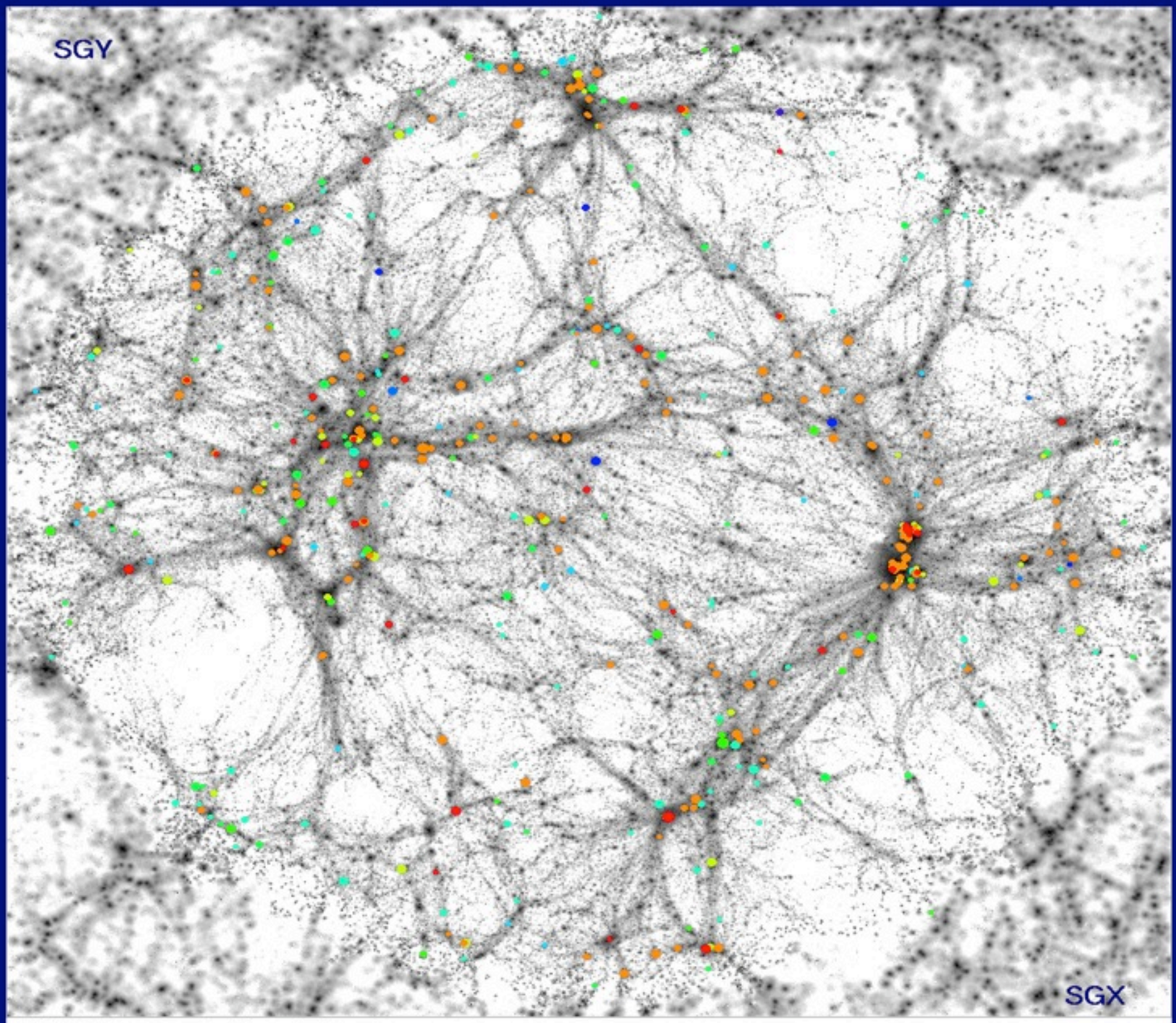

ΛCDM CR : E and S0 galaxies
Credits : Mathis, Lemson, Springel, Kauffmann, White and Dekel.

Formation of galaxies in a cluster

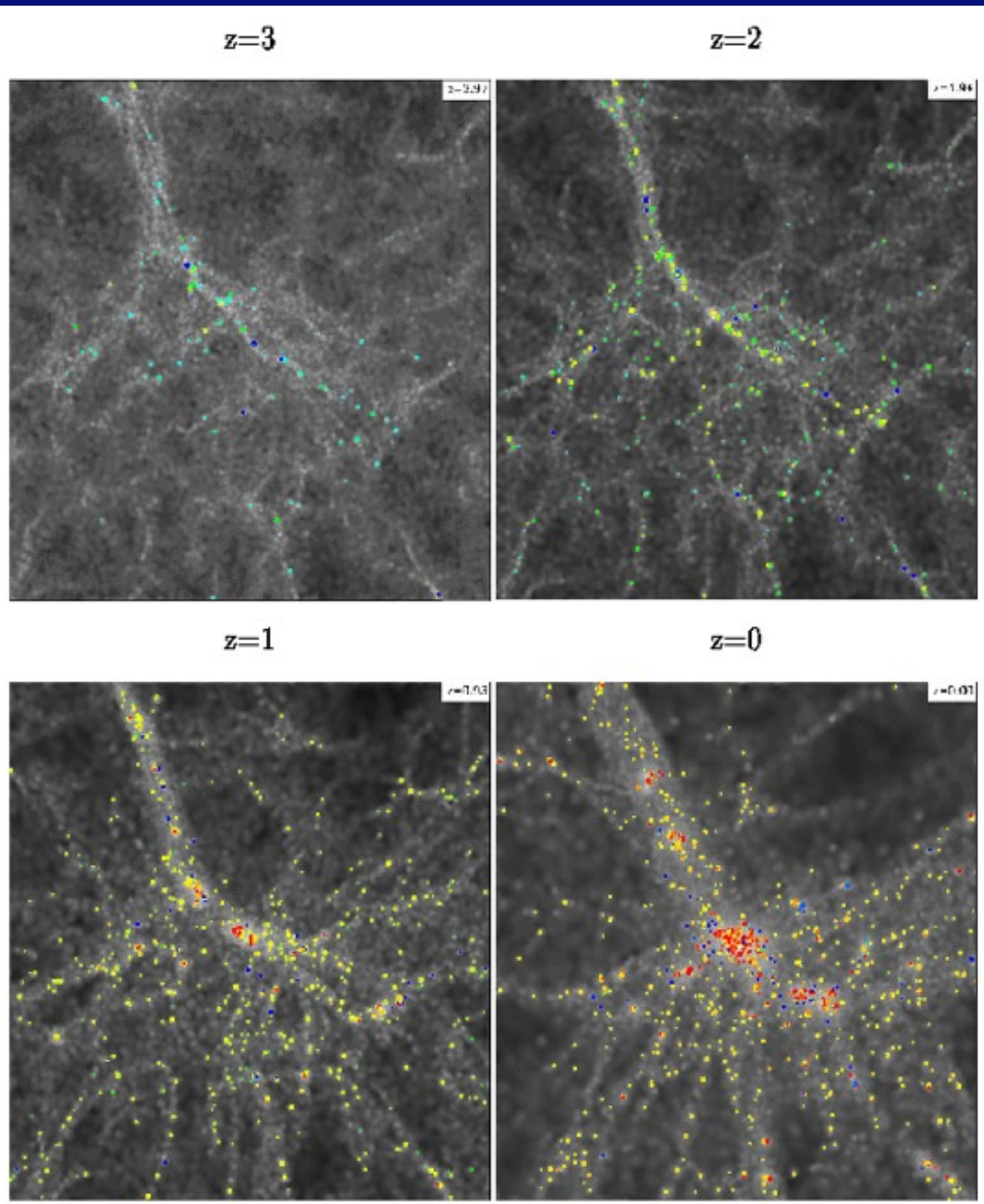

1 Gpc/h

Millennium Simulation

10.077.696.000 particles

(z = 0)

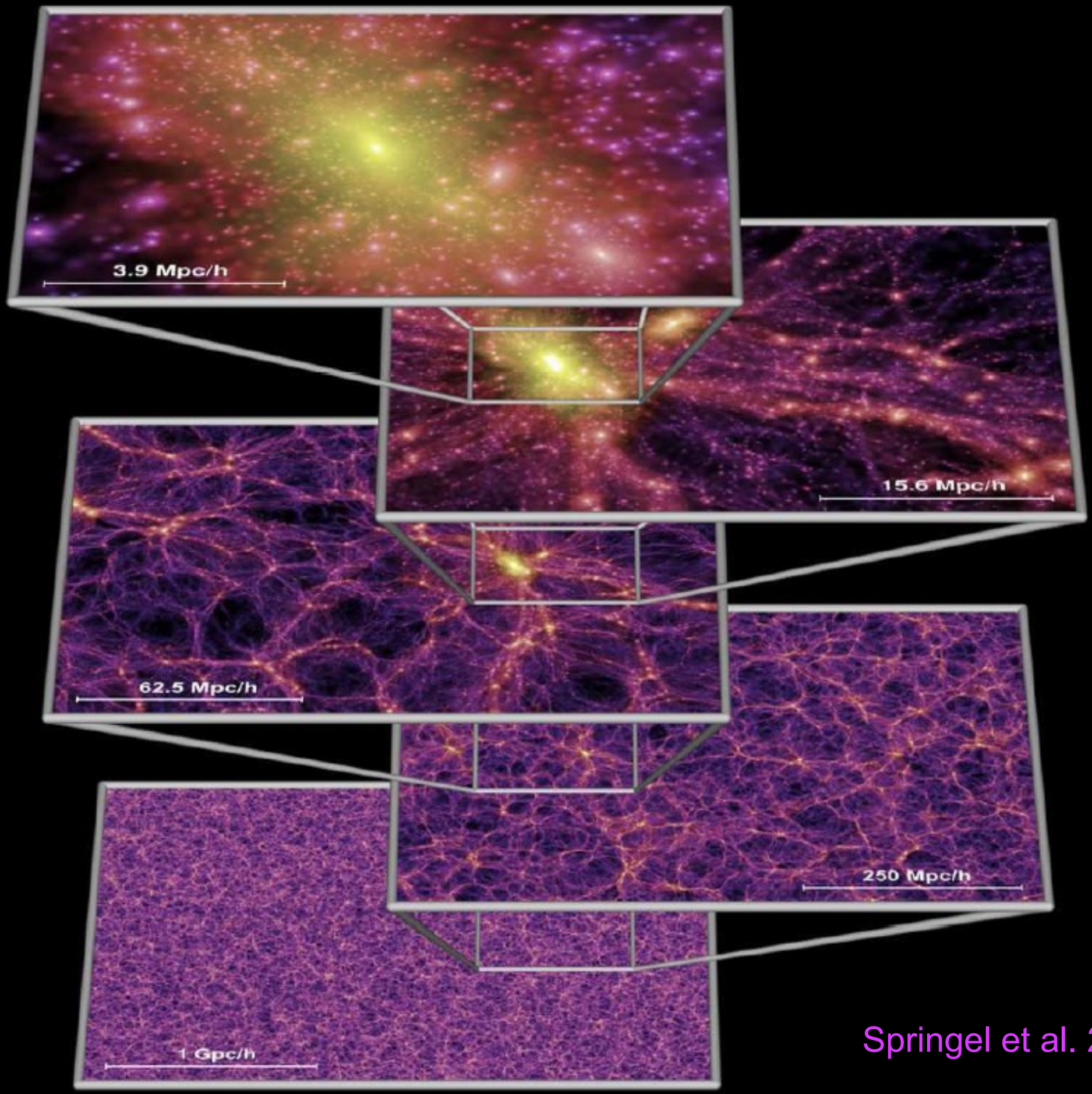

Springel et al. 2005

Millennium Simulation

Environment of a ‘first quasar candidate’ at high and low redshifts. The two panels on the left show the projected dark matter distribution in a cube of comoving sidelength $10h^{-1}$ Mpc, colour-coded according to density and local dark matter velocity dispersion. The panels on the right show the galaxies of the **semi-analytic model** overlayed on a gray-scale image of the dark matter density. The volume of the sphere representing each galaxy is proportional to its stellar mass, and the chosen colours encode the restframe stellar $B-V$ colour index. While at $z = 6.2$ (top) all galaxies appear blue due to ongoing star formation, many of the galaxies that have fallen into the rich cluster at $z = 0$ (bottom) have turned red.

Springel et al. 2005

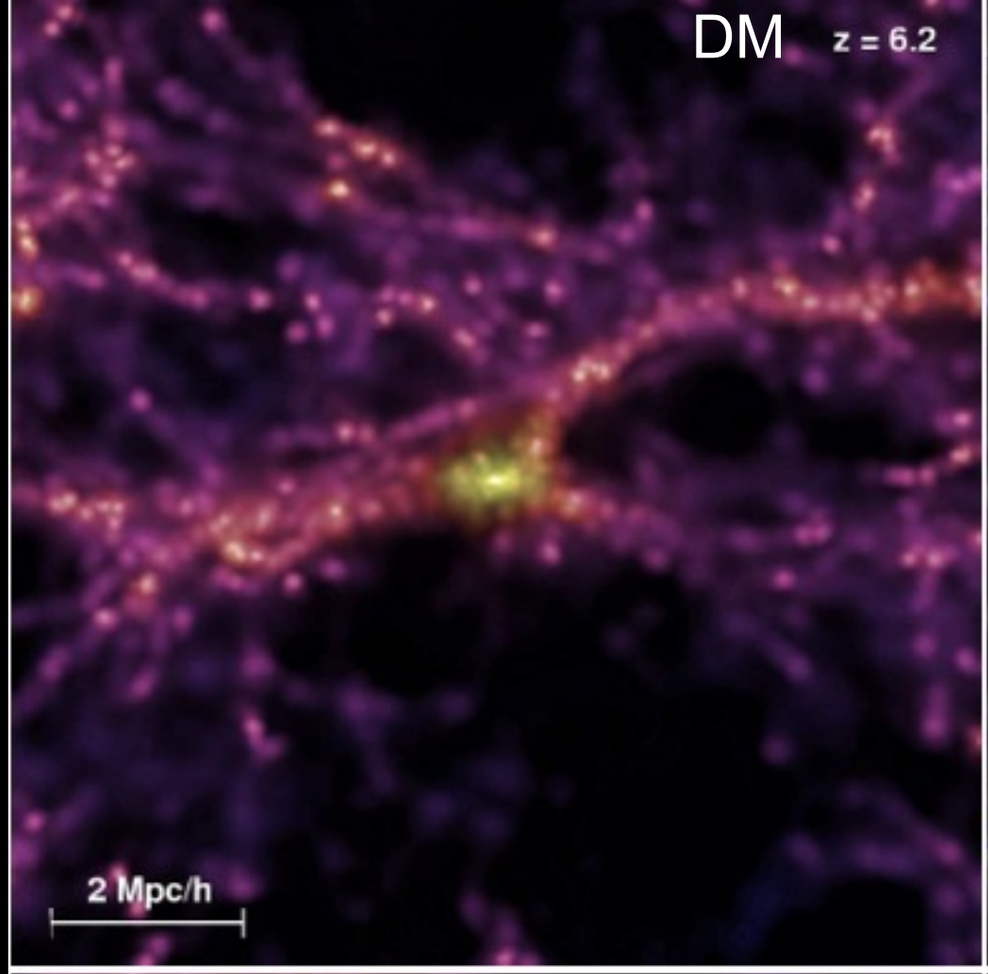

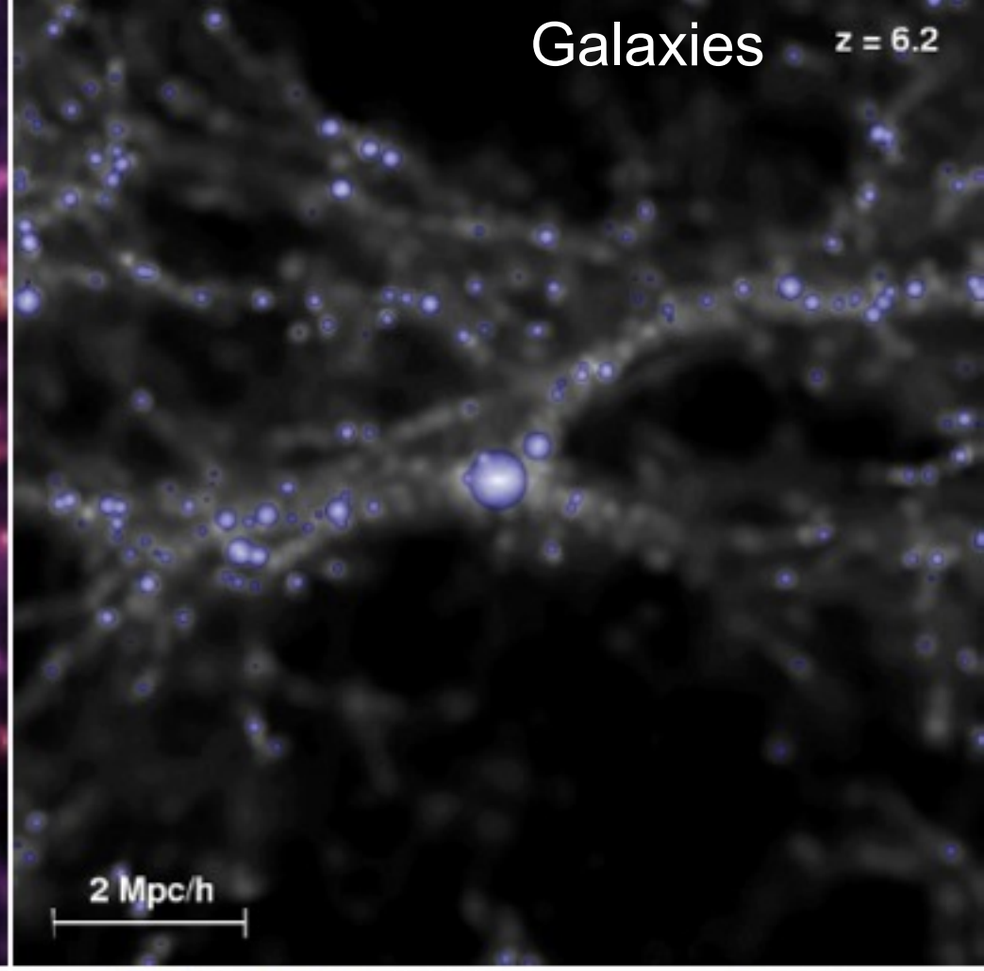

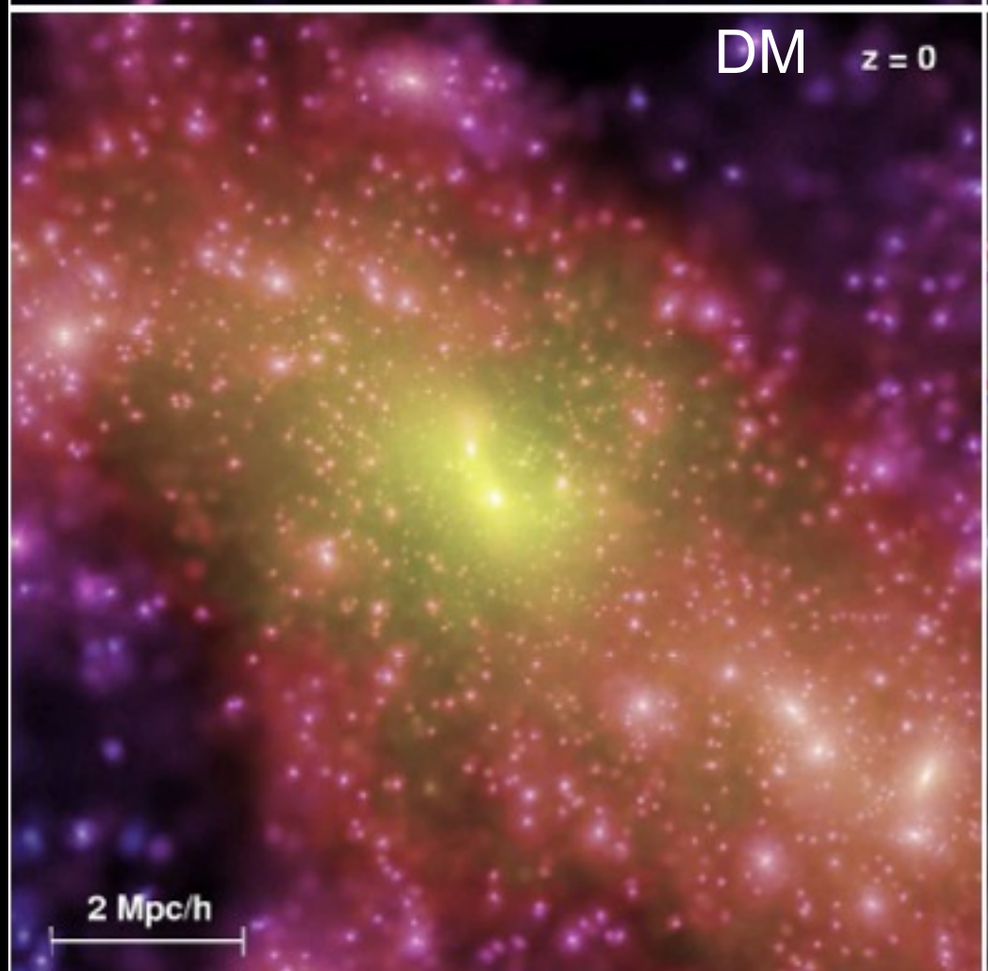

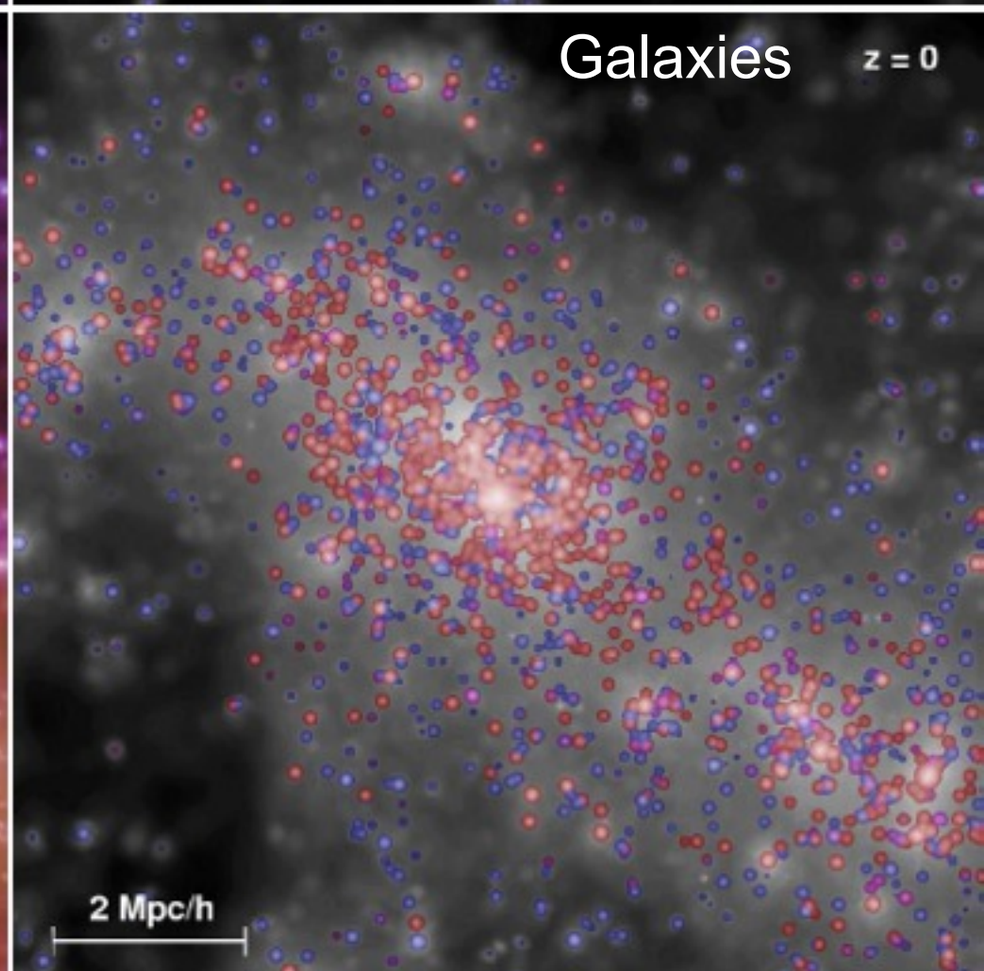

Semi-Analytic Models of Galaxy Formation

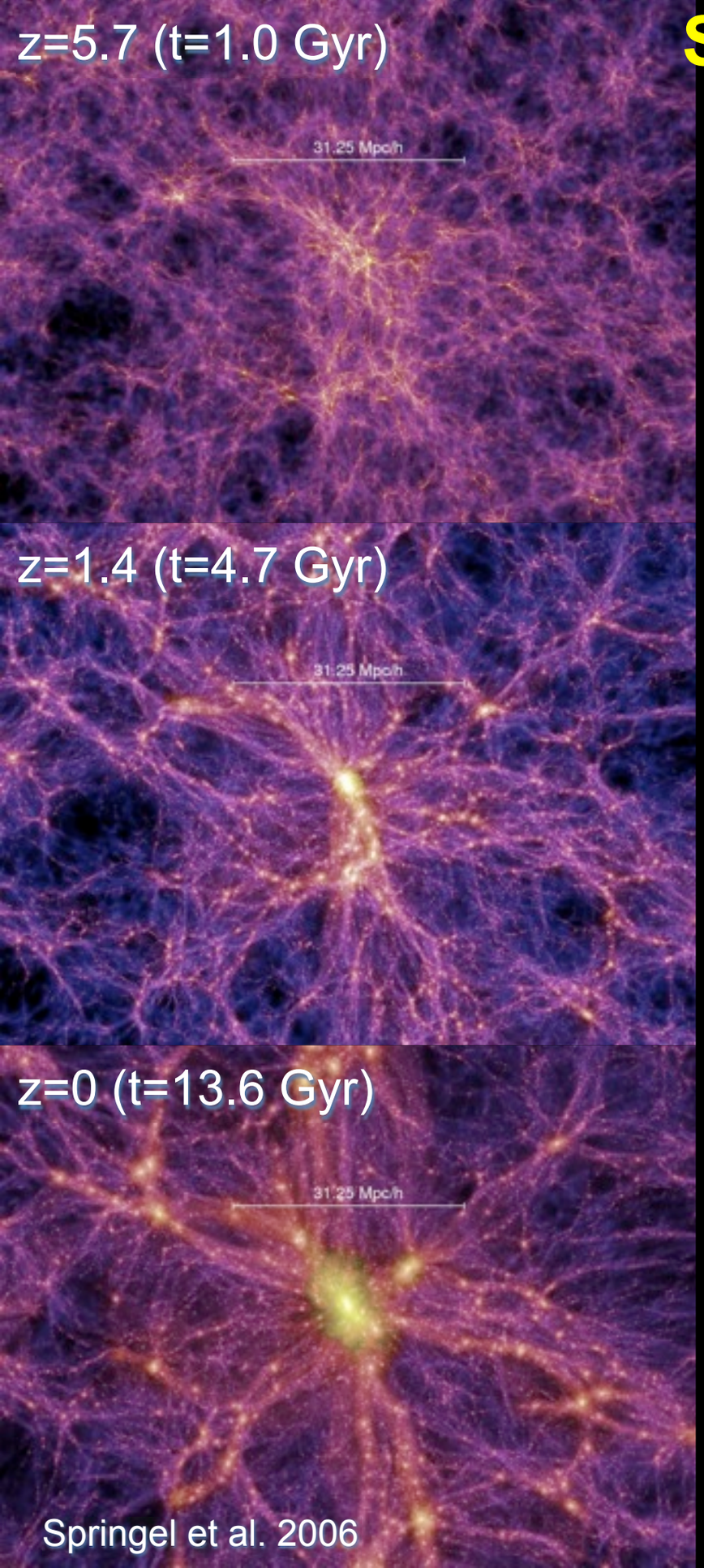

Springel et al. 2006

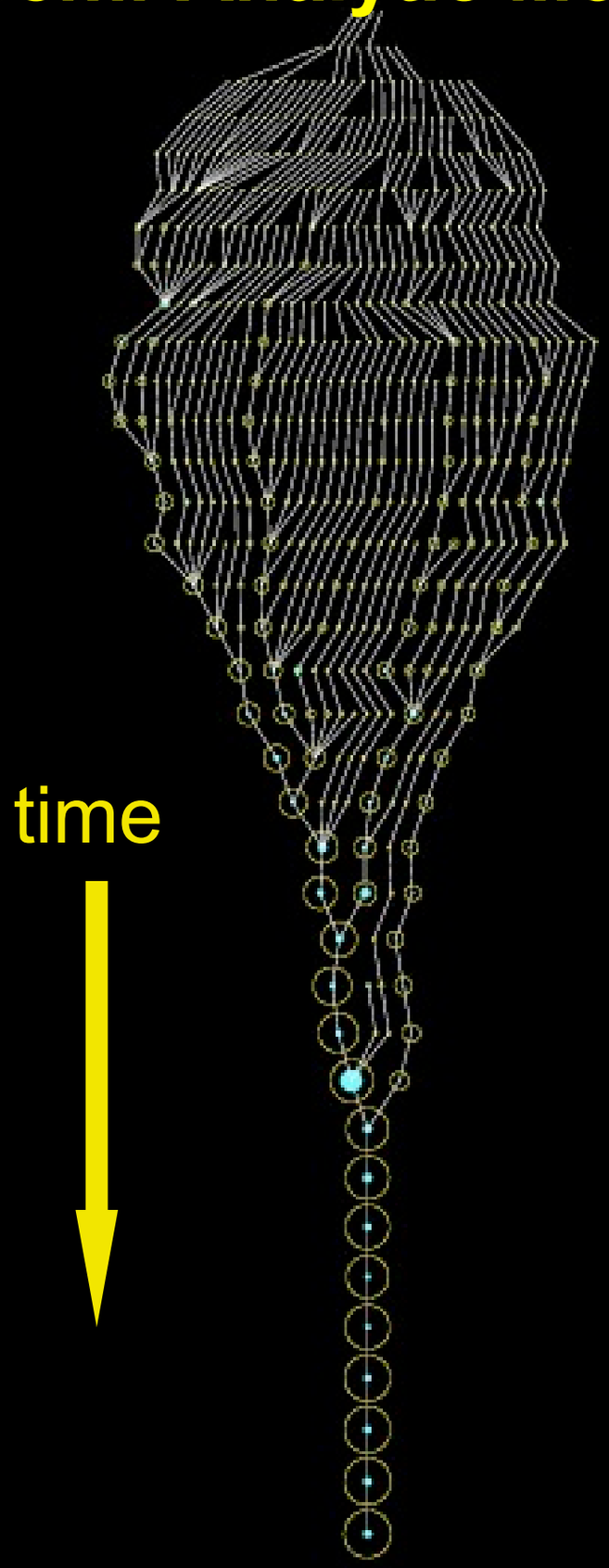

Wechsler et al. 2002

Present status of ΛCDM "Double Dark" theory:

- cosmological parameters are now well constrained by observations
- structure formation in dominant dark matter component accurately quantified
- mass accretion history of dark matter halos is represented by 'merger trees' like the one at left

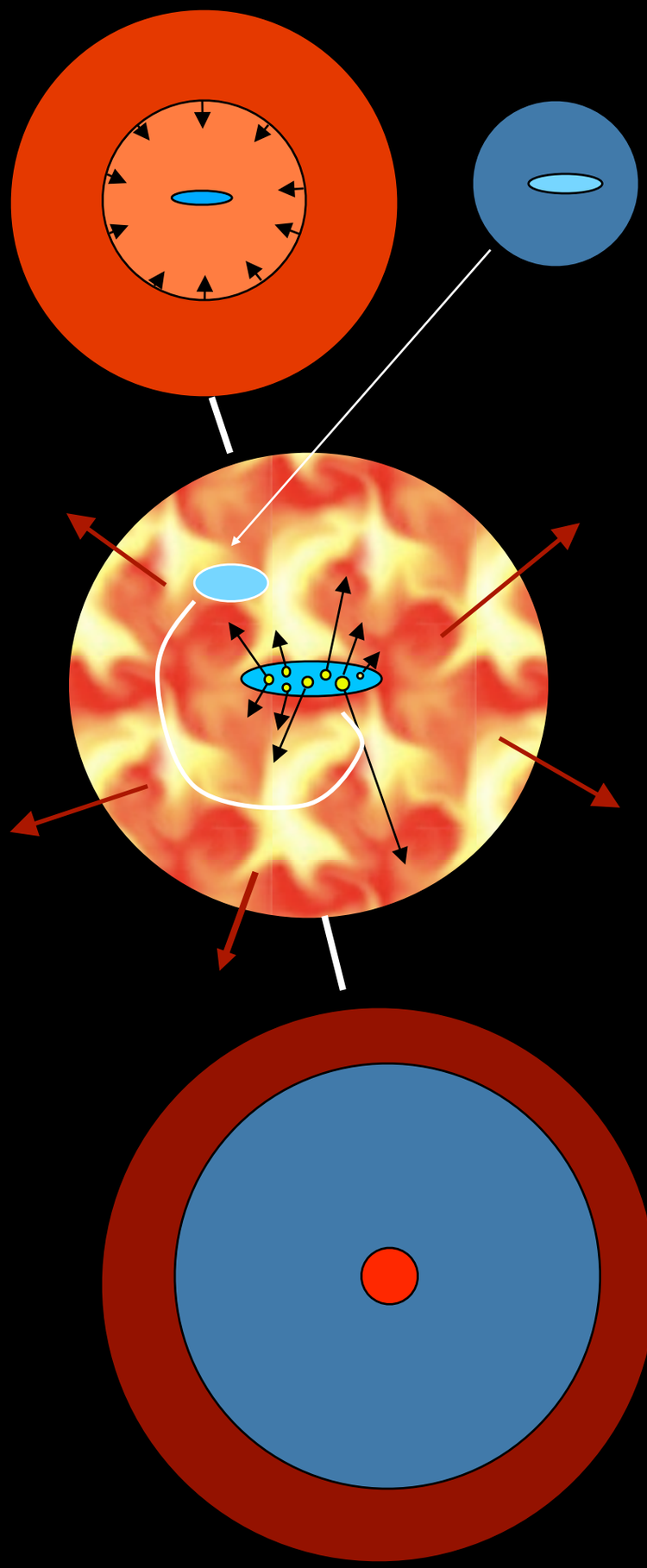

Semi-Analytic Models of Galaxy Formation

- gas is collisionally heated when perturbations ‘turn around’ and collapse to form gravitationally bound structures
- gas in halos cools via atomic line transitions (depends on density, temperature, and metallicity)
- cooled gas collapses to form a rotationally supported disk
- cold gas forms stars, with efficiency a function of gas density (e.g. Schmidt-Kennicutt Law)
- massive stars and SNae reheat (and expel?) cold gas and some metals
- galaxy mergers trigger bursts of star formation; ‘major’ mergers transform disks into spheroids

White & Frenk 1991; Kauffmann et al. 93; Cole et al. 94; Somerville & Primack 99; Cole et al. 2000; Somerville, Primack, & Faber 01; Croton et al. 06; De Lucia & Blaizot 06; Cattaneo et al. 07; Somerville et al. 08

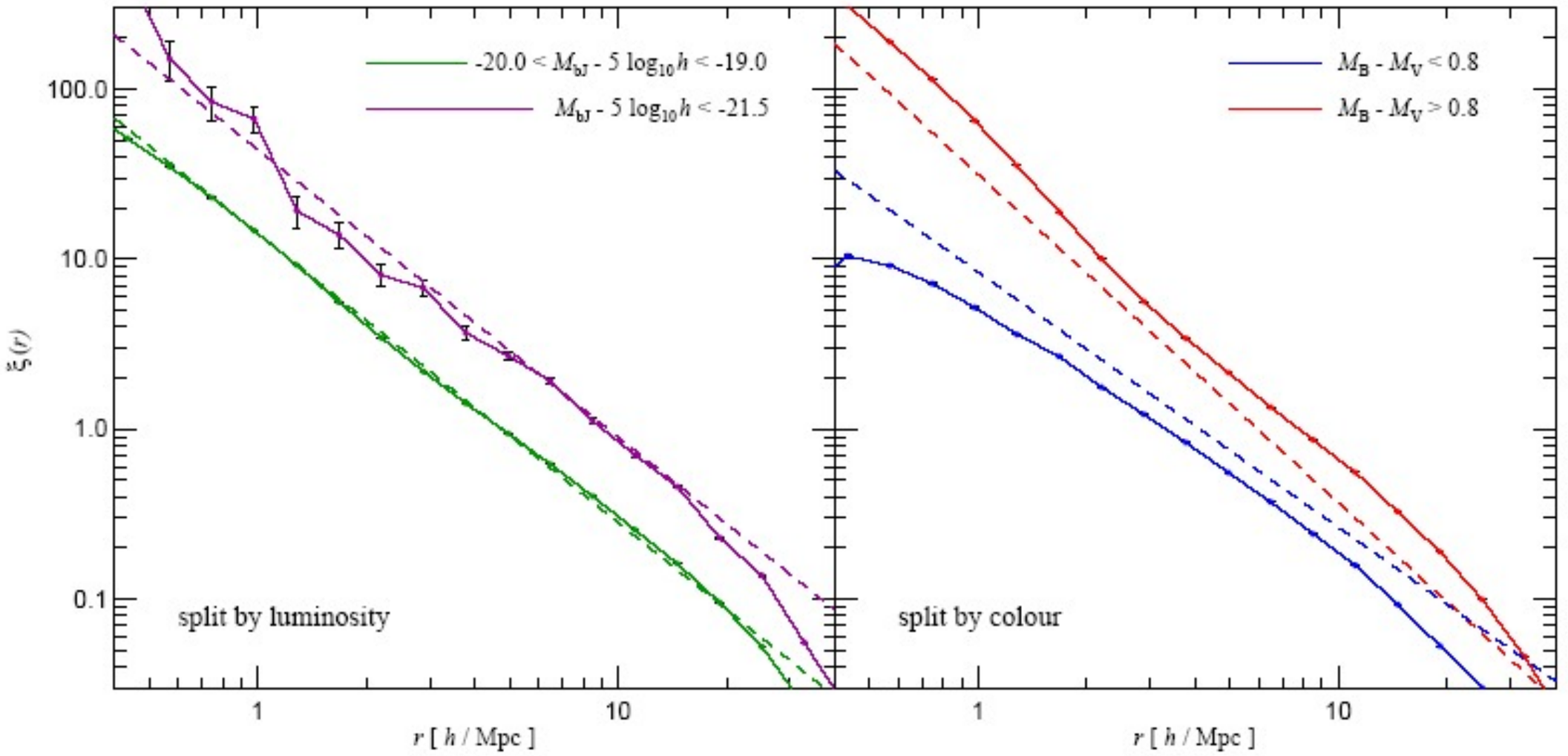

Figure 5: Galaxy clustering as a function of luminosity and colour. In the panel on the left, we show the 2-point correlation function of our galaxy catalogue at $z = 0$ split by luminosity in the bJ-band (symbols). Brighter galaxies are more strongly clustered, in quantitative agreement with observations[33] (dashed lines). Splitting galaxies according to colour (right panel), we find that red galaxies are more strongly clustered with a steeper correlation slope than blue galaxies. Observations[35] (dashed lines) show a similar trend, although the difference in clustering amplitude is smaller than in this particular semi-analytic model.

Springel et al. 2005

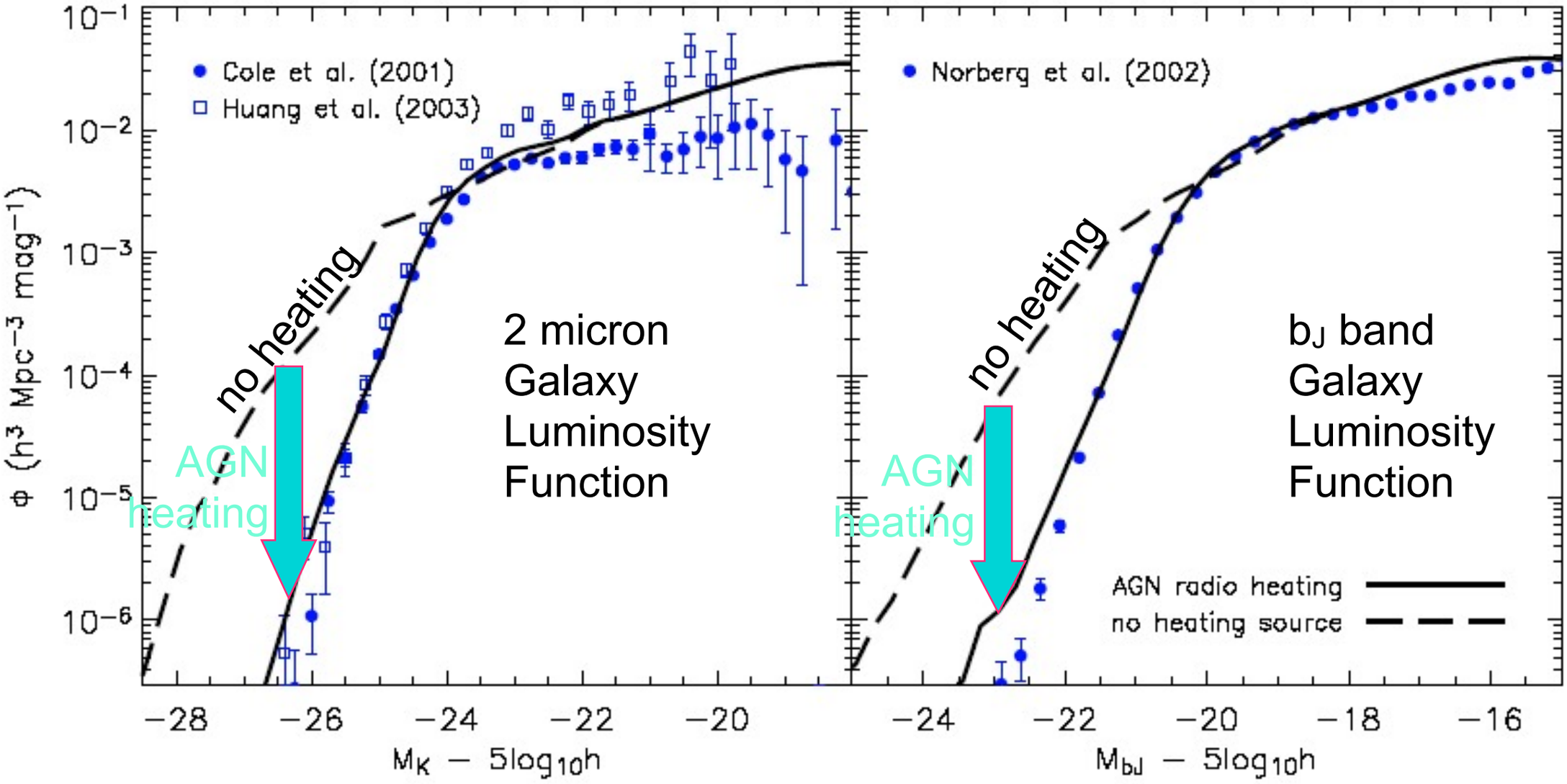

Figure 8. Galaxy luminosity functions in the K (left) and b_J (right) photometric bands, plotted with and without 'radio mode' feedback (solid and long dashed lines respectively – see Section 3.4). Symbols indicate observational results as listed in each panel. As can be seen, the inclusion of AGN heating produces a good fit to the data in both colours. Without this heating source our model overpredicts the luminosities of massive galaxies by about two magnitudes and fails to reproduce the sharp bright end cut-offs in the observed luminosity functions.

Croton et al. 2006

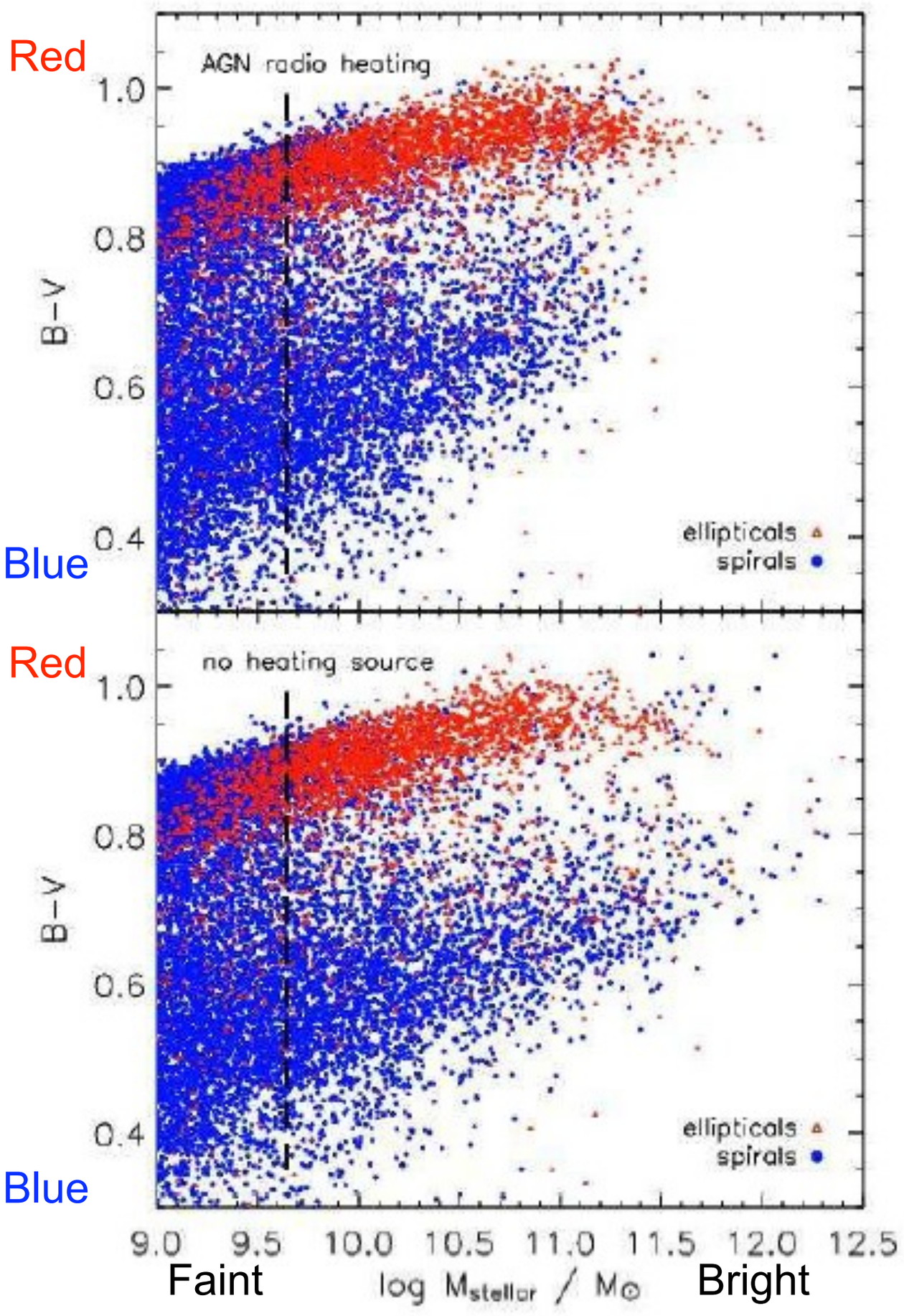

Color Magnitude Diagram

With AGN heating – brightest galaxies are red, as observed

Without heating – brightest galaxies are blue

Croton et al. 2006

(see also Cattaneo et al. 2006)

Baryons in Dark Matter Halos

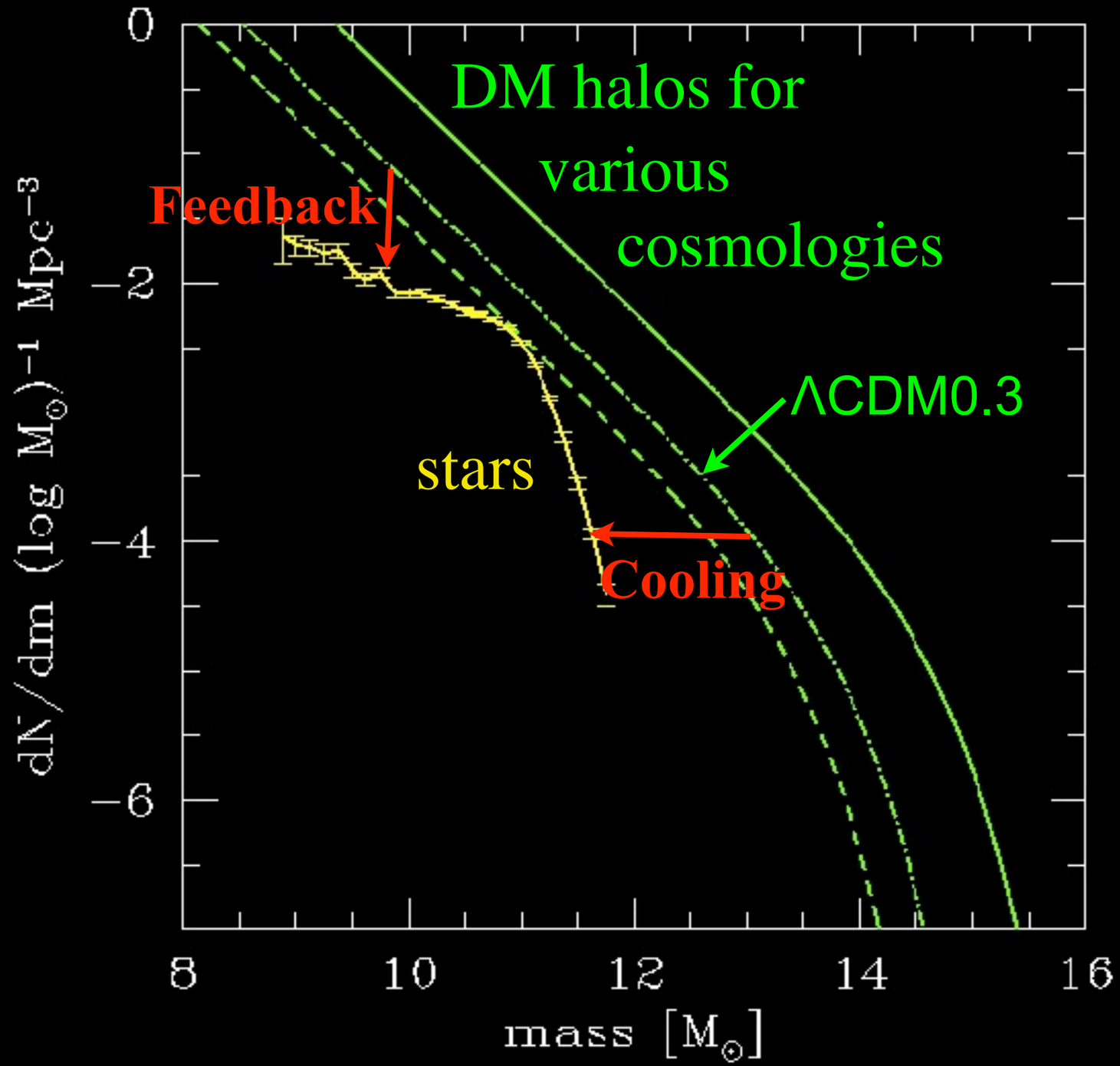

- in order to reconcile CDM (sub)halo mass function with galaxy LF or stellar MF, cooling/star formation must be inefficient overall, most efficient at $M_{halo} \sim 10^{11}\ M_{sun}$
- baryon/DM ratio must be a strongly non-linear (& non-monotonic) function of halo mass

Somerville & Primack 1999; cf. Benson et al. 2003

Dark halo mass growth vs. time: 4 clusters

GALics DM halos by Cattaneo et al. 2006

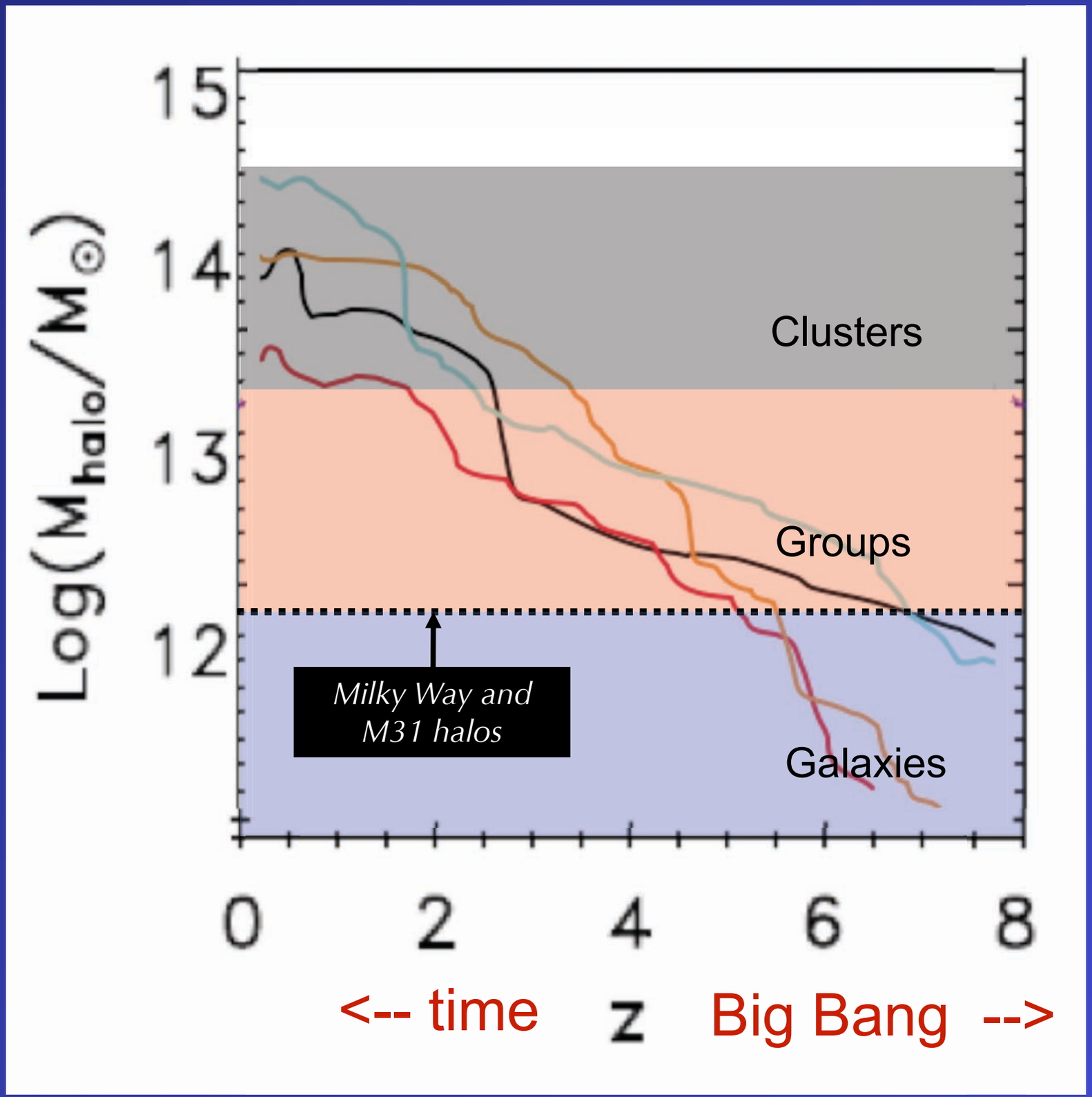

Dark halos of progressively smaller mass

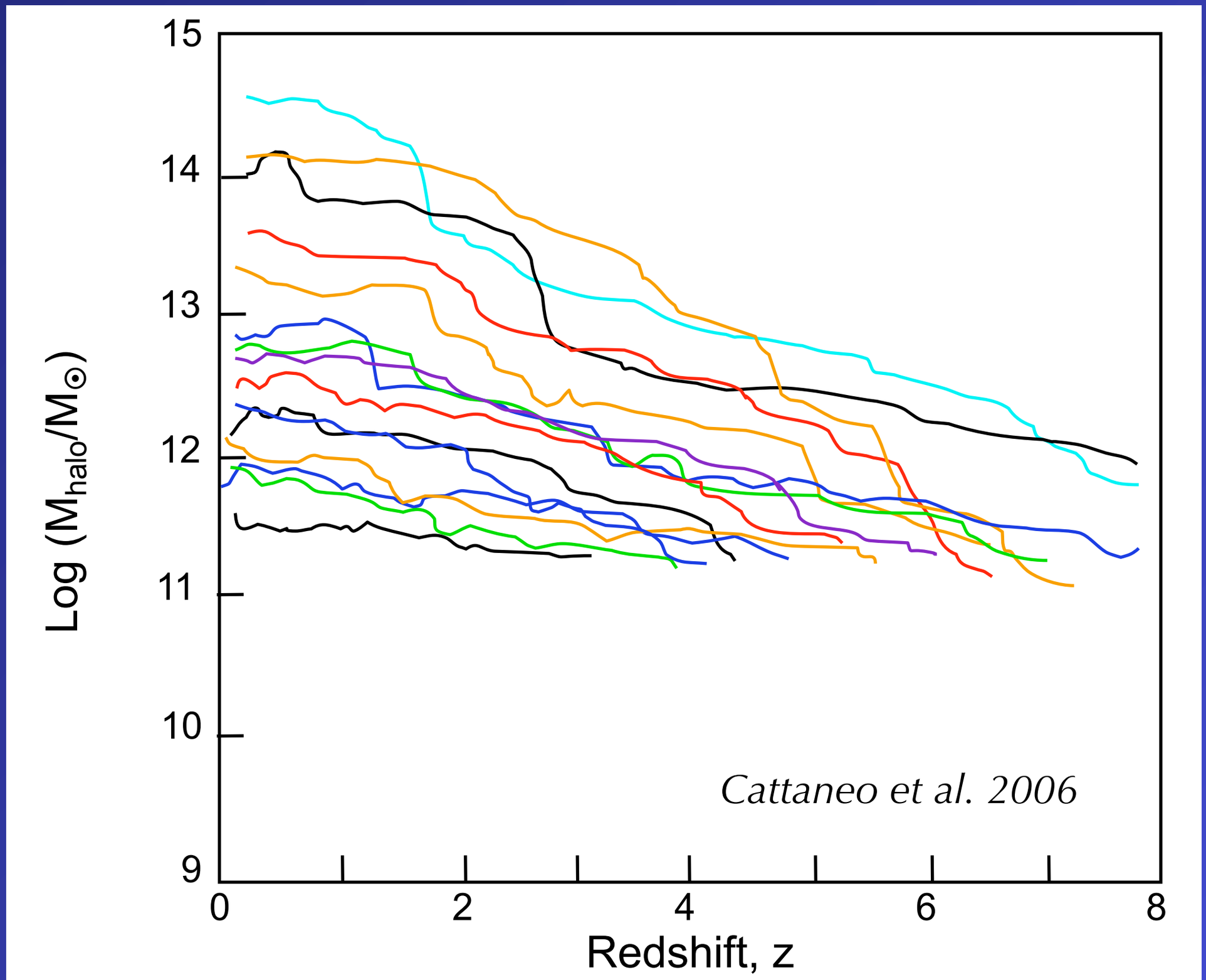

A schematic model of average halo mass growth

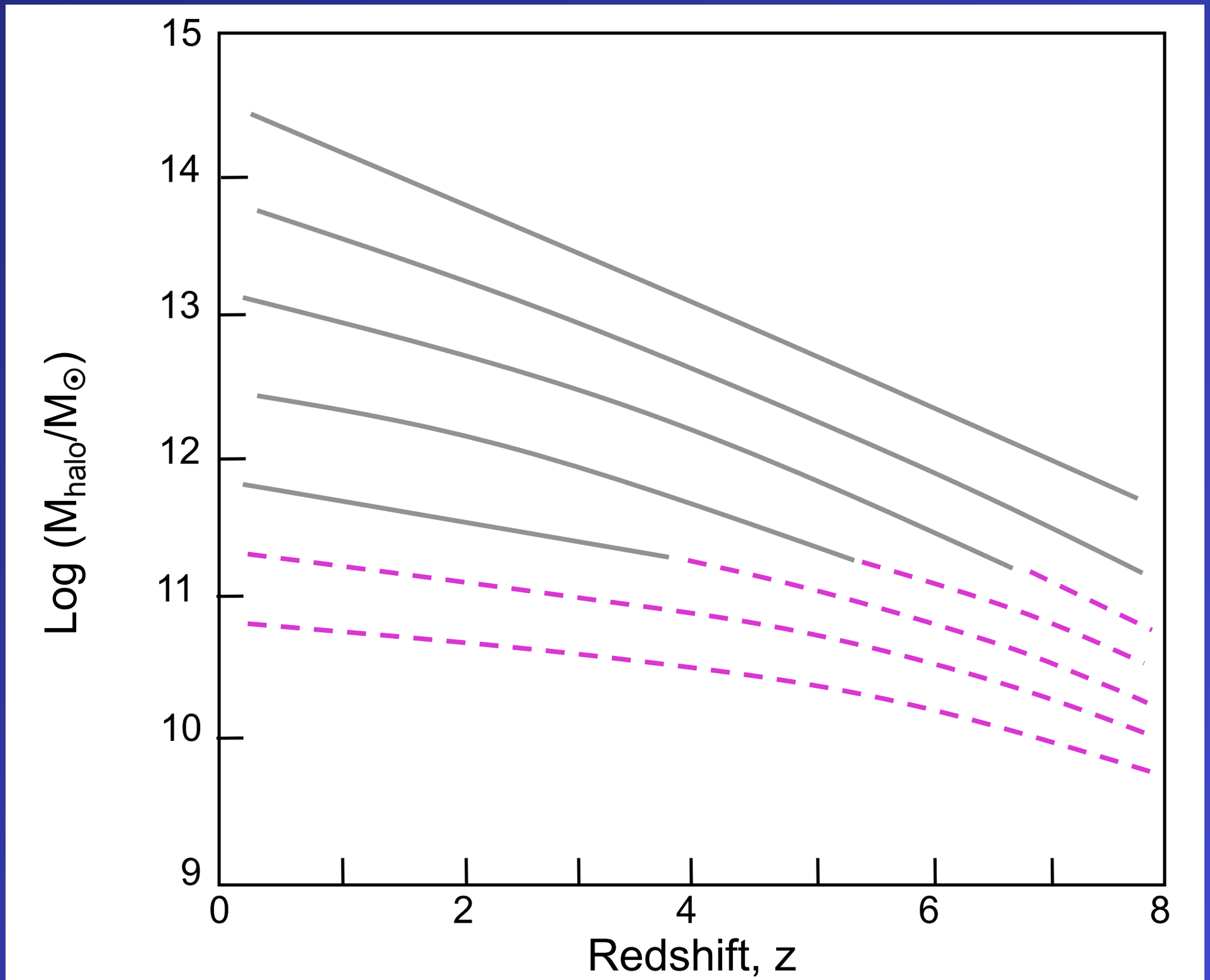

Key assumption: ***star-forming band*** in dark-halo mass

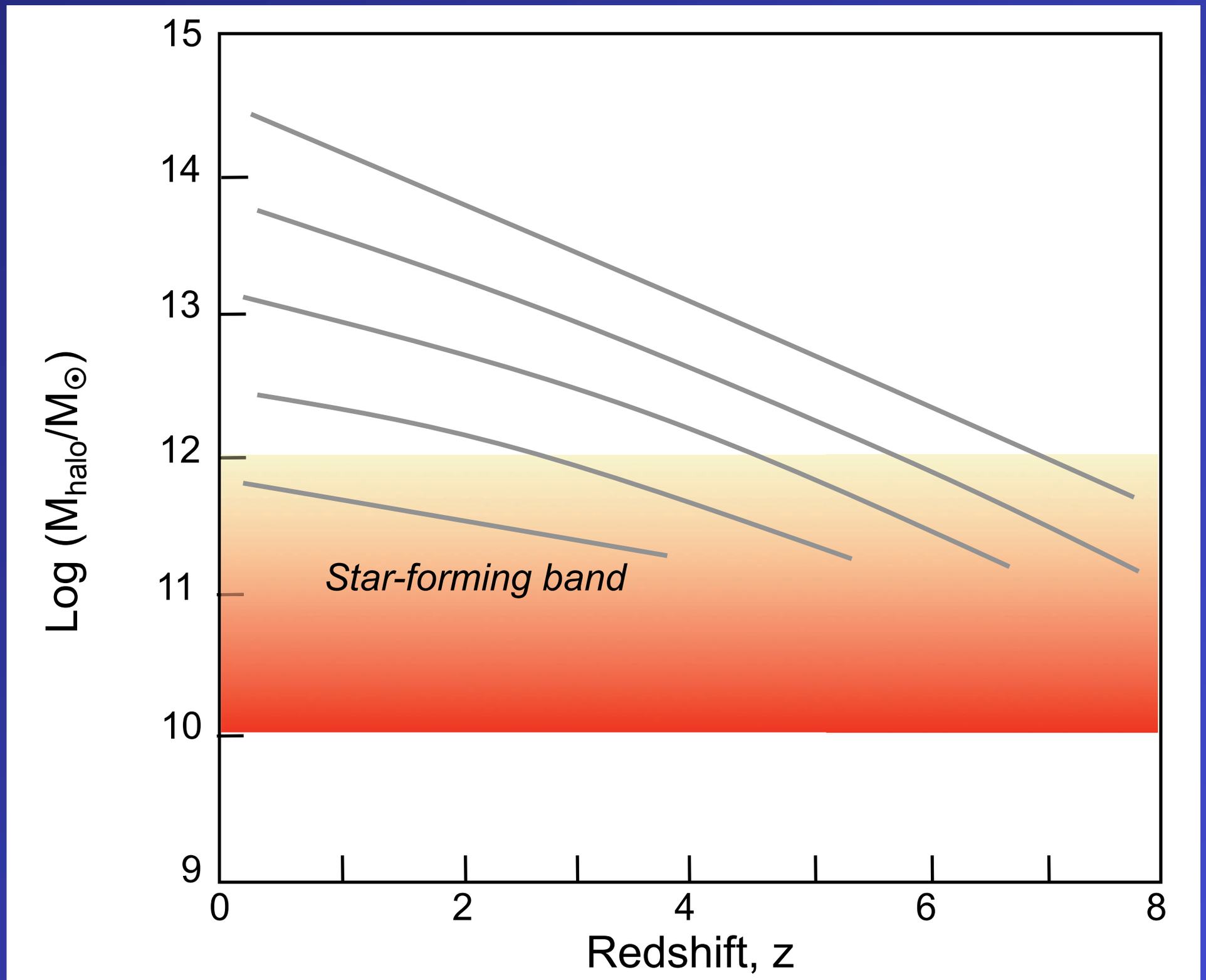

Key assumption: ***star-forming band*** in dark-halo mass

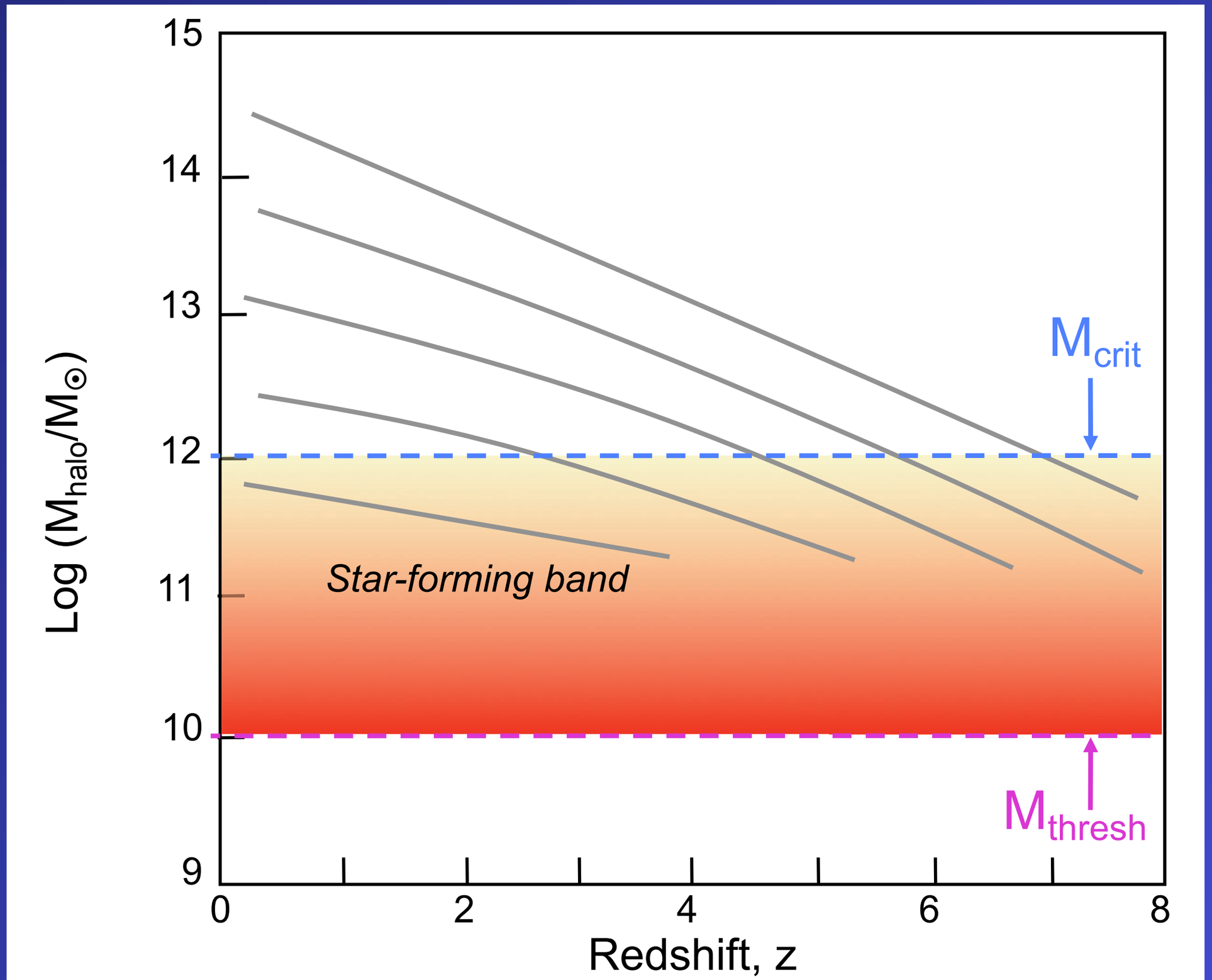

Hydro simulations with gas + dark matter switch from ***cold flows*** to ***hot bubbles*** at $M_{crit} \sim 10^{12}\ M_\odot$

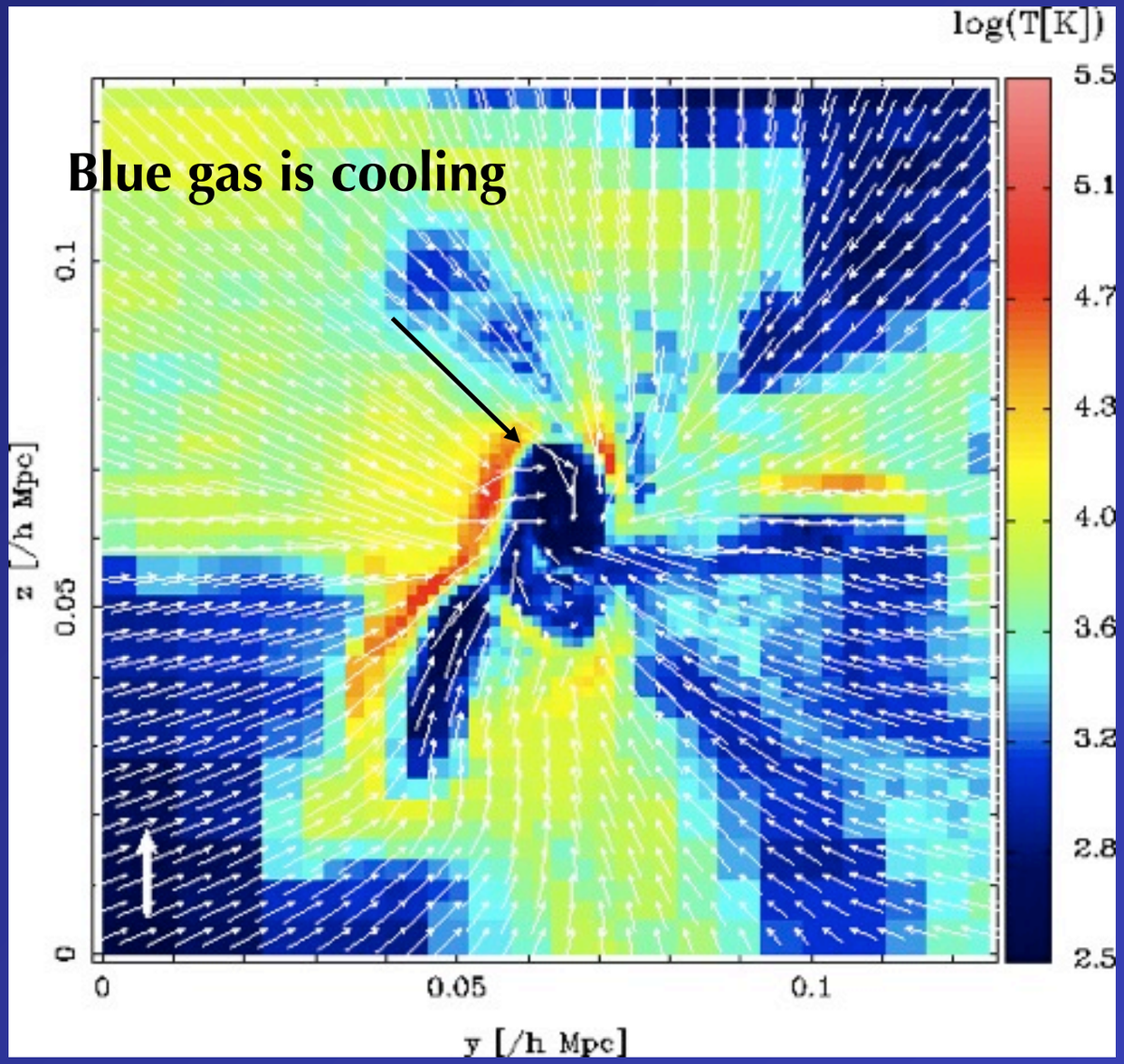

Small halo mass = $10^{11}\ M_\odot$

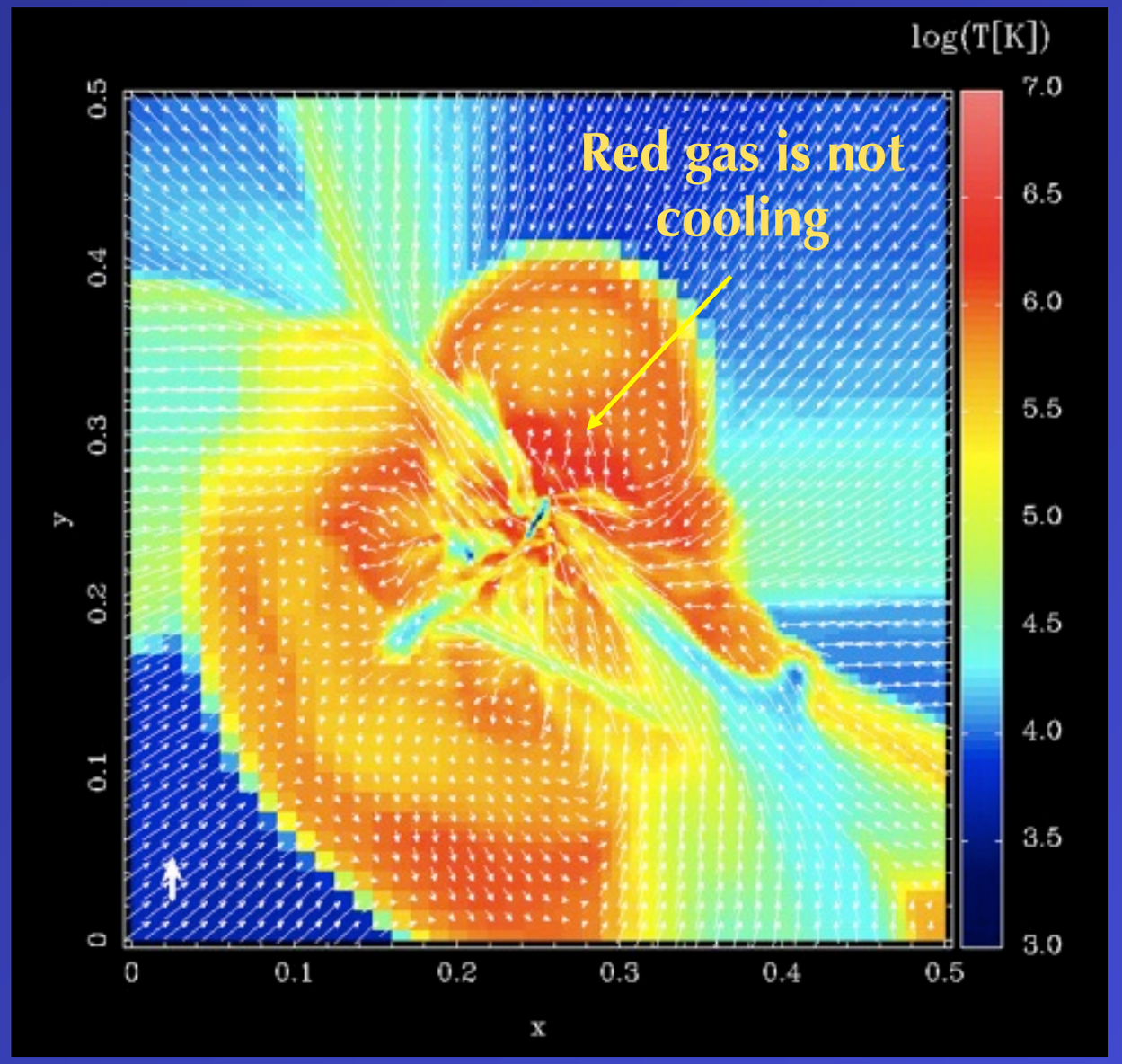

Large halo mass = $10^{13}\ M_\odot$

Dekel & Birnboim 2006

Hydrodynamic simulations by Andrei Kravtsov

Key assumption: ***star-forming band*** in dark-halo mass

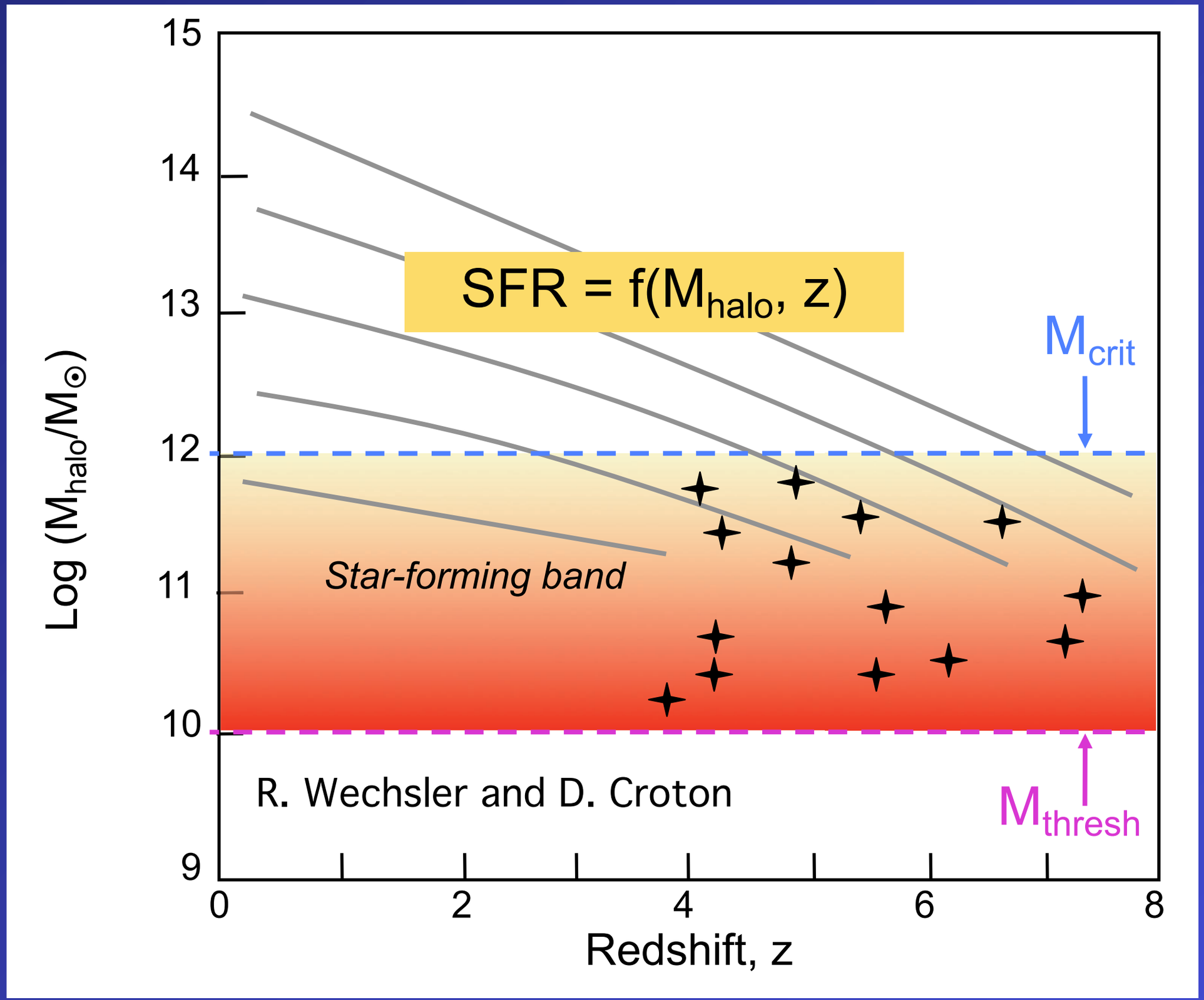

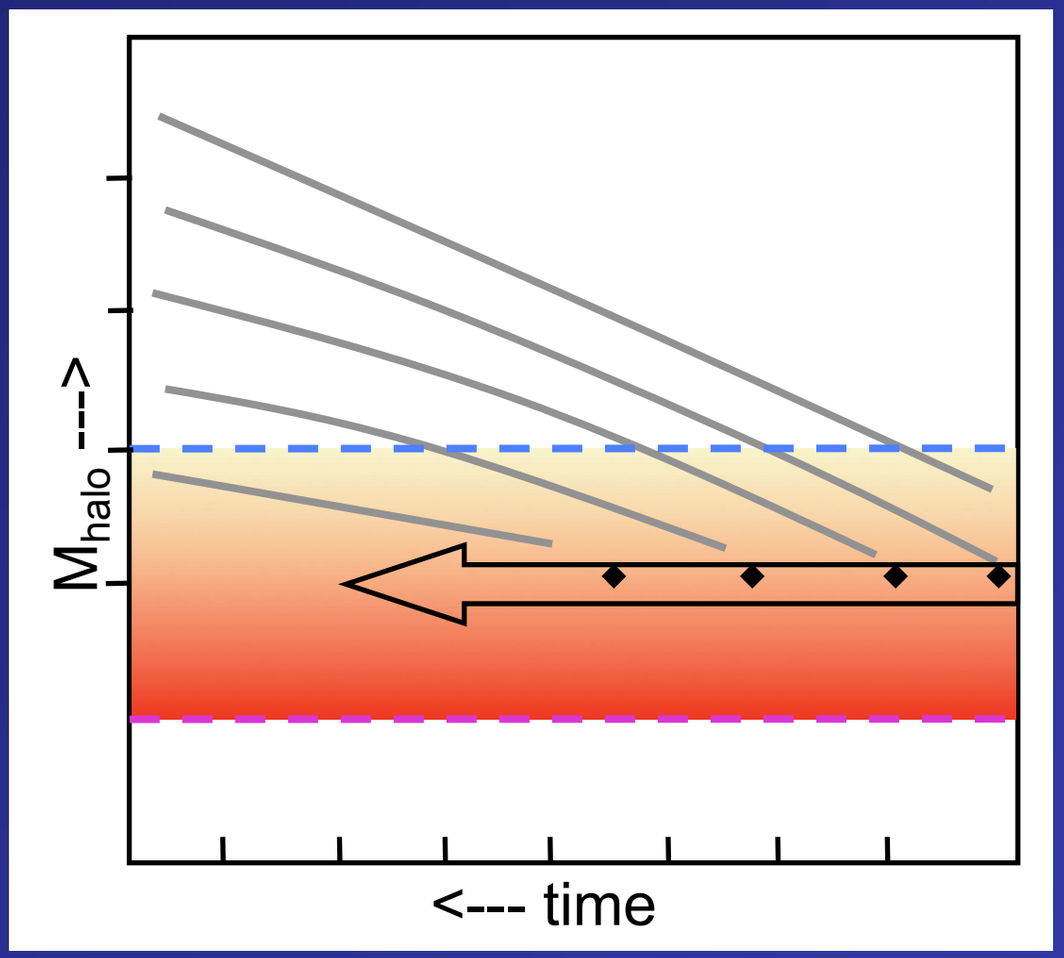

Implications and Predictions of the Model

1) Each halo has a unique dark-matter growth path and associated stellar mass growth path.

2) Stellar mass follows halo mass until M_{halo} crosses M_{crit}.

SAMs: $M_{star} < 0.05\ M_{halo}$

3) A ***mass sequence*** comes from the fact that different halo masses enter the star-forming band at different times. A galaxy's position is determined by its ***entry redshift*** into the band. More massive galaxies enter earlier. Thus:

$$z_{entry} \leftrightarrow M_{halo} \leftrightarrow M_{star}$$

Sandra Faber

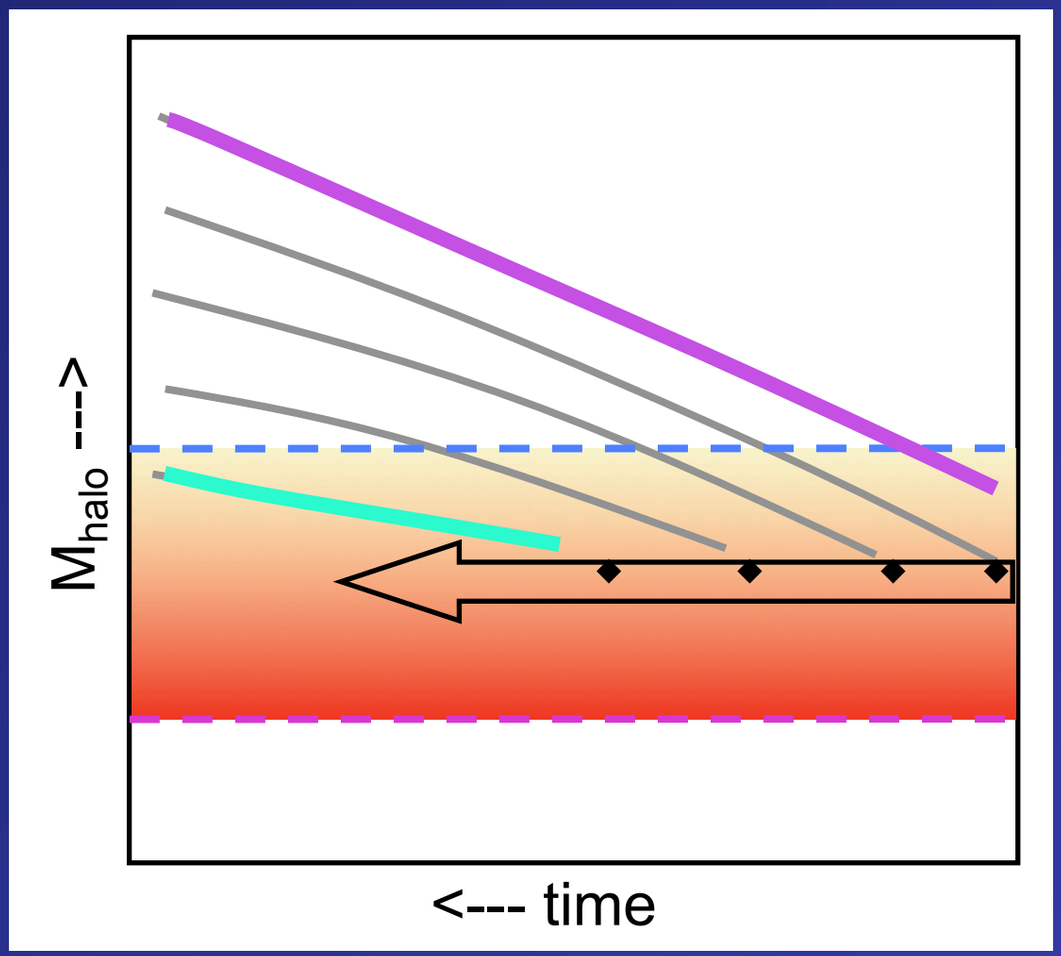

Implications and Predictions of the Model

Massive galaxies:

- Started forming stars early.
- Shut down early.
- Are red today.
- Populate dark halos that are much more massive than their stellar mass.

Small galaxies:

- Started forming stars late.
- Are still making stars today.
- Are blue today.
- Populate dark halos that match their stellar mass.

"Downsizing"

Star formation is a wave that started in the largest galaxies and swept down to smaller masses later (Cowie et al. 1996).

Sandra Faber

Theories for the ***upper*** halo star-formation boundary

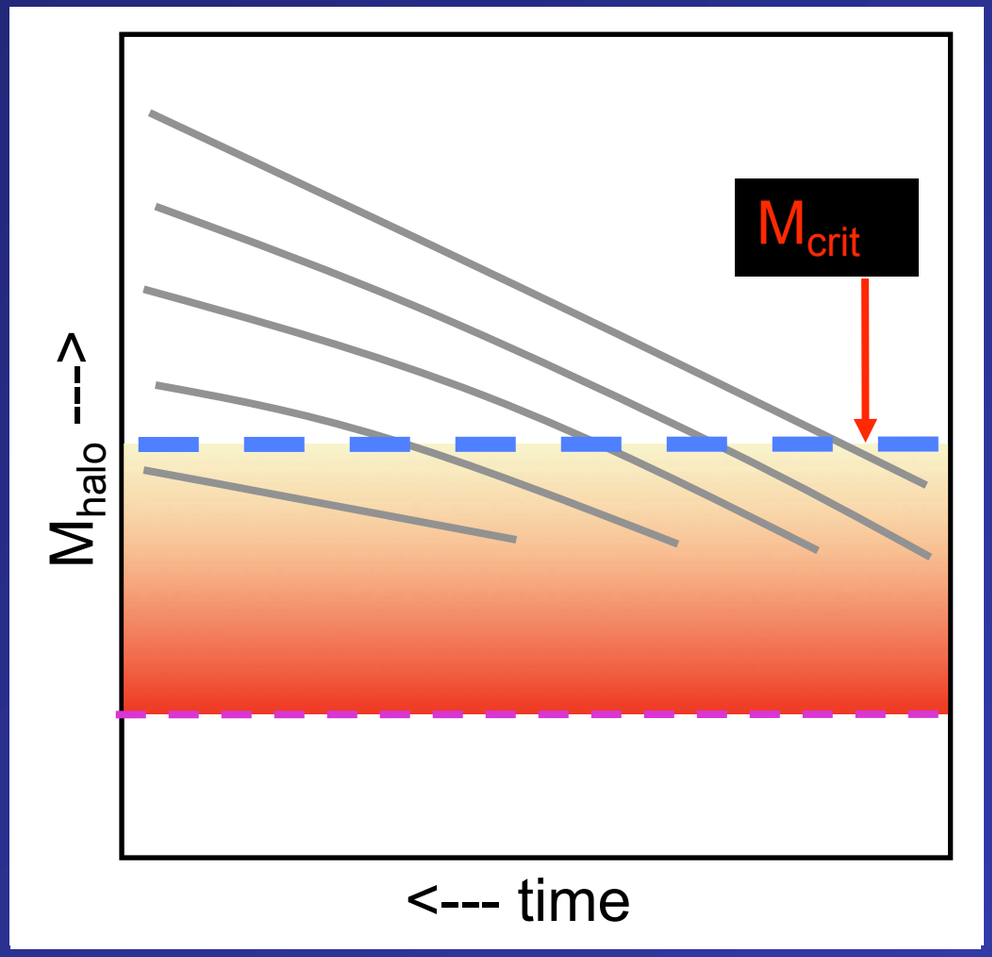

M_{crit} is the halo mass at the UPPER edge of the star-formation band, roughly 10^{12} M_W

1. Gas in halos above the critical halo mass M_{crit} ~ 10^{12} $M_\odot$ cannot cool (Ostriker & Rees 1978, Blumenthal et al. 1984, Dekel & Birnboim 2007).

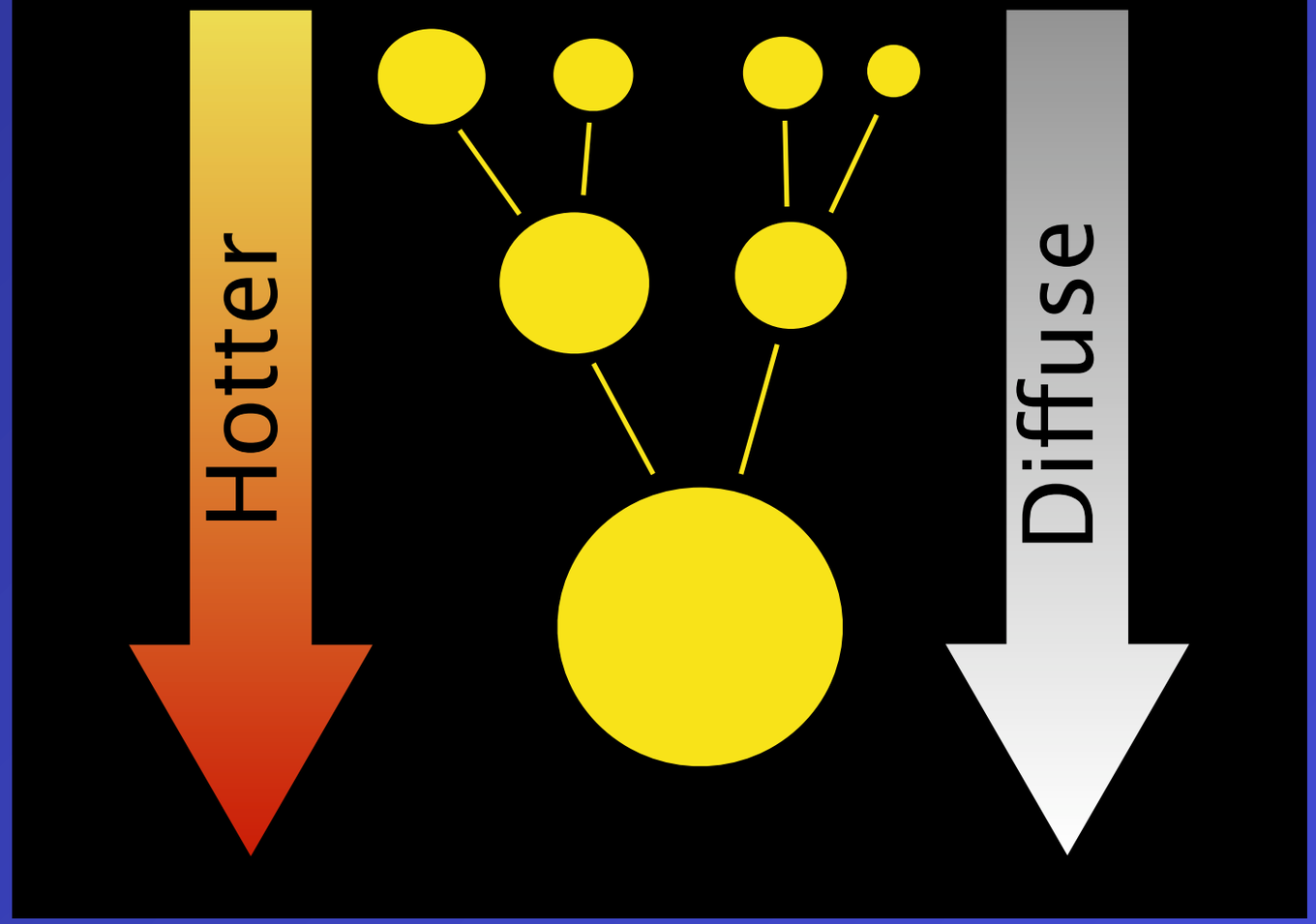

Theories for the ***lower*** halo star-formation boundary

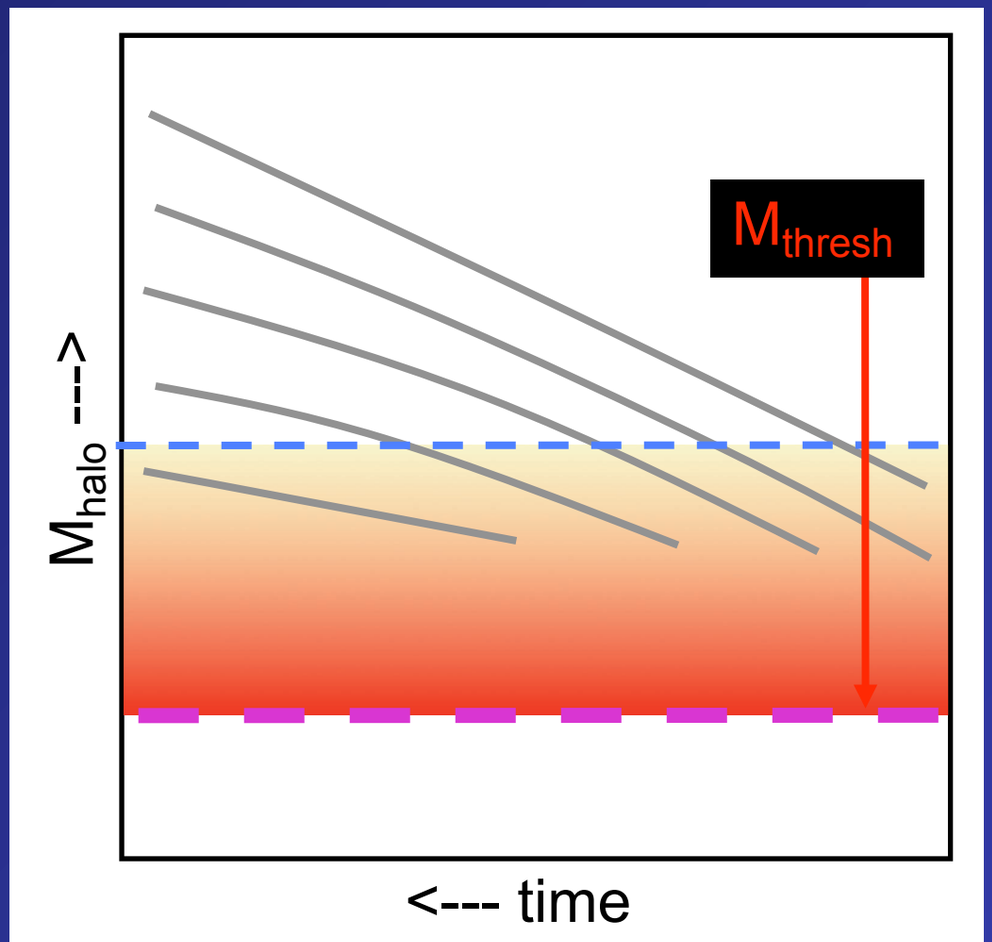

M_{thresh} is the halo mass at the LOWER edge of the star-formation band, roughly 10^{10} $M_{\odot}$.

Not yet well understood

1. Supernova feedback (Dekel & Silk 1985):

   $v_{lim} < 100$ km/sec

2. Early Universe reionization (e.g., Somerville 2002):

   $v_{lim} < 30$ km/sec

3. Plus tidal destruction!

More realistic model of halo-cooling boundary

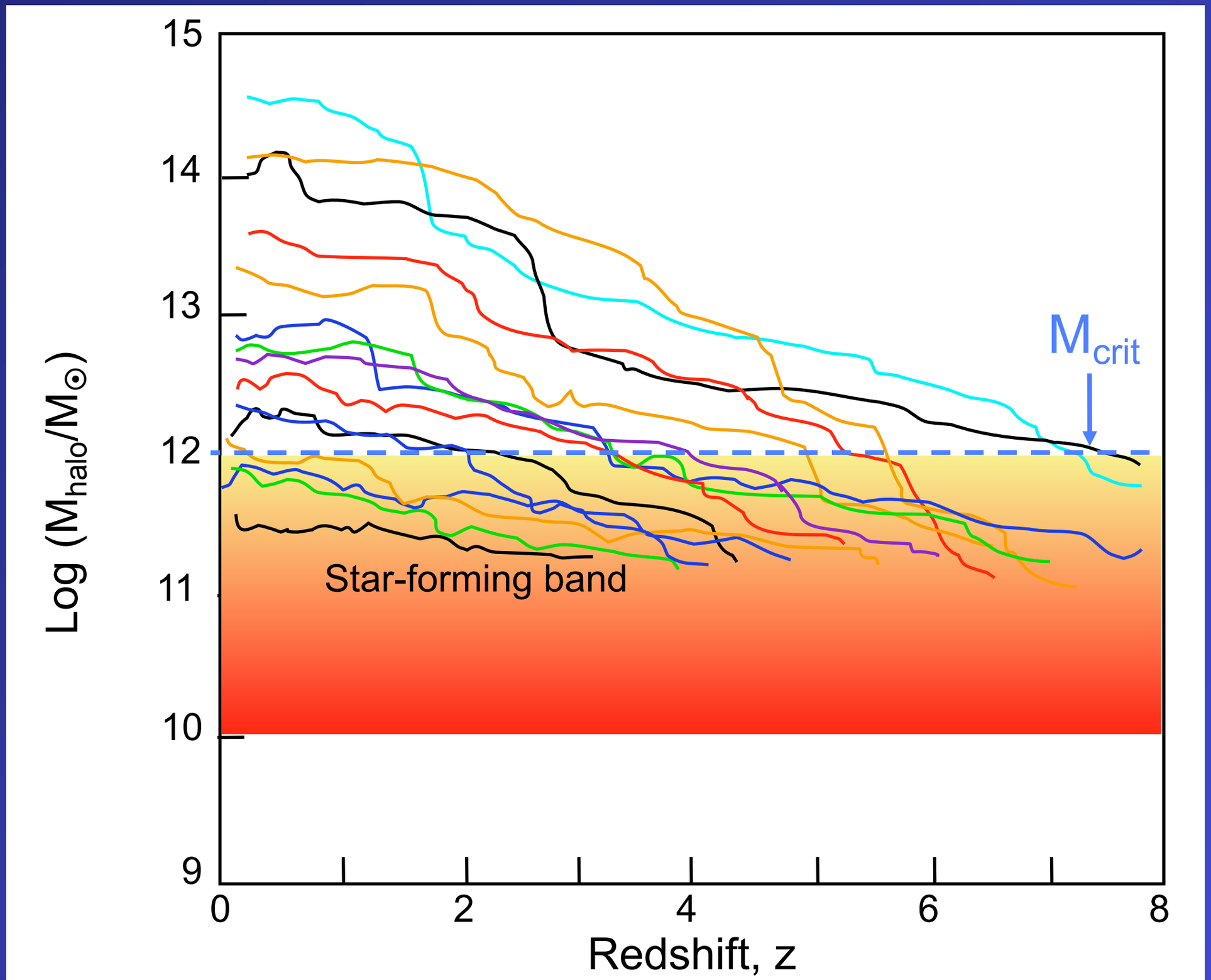

More realistic model of halo-cooling boundary

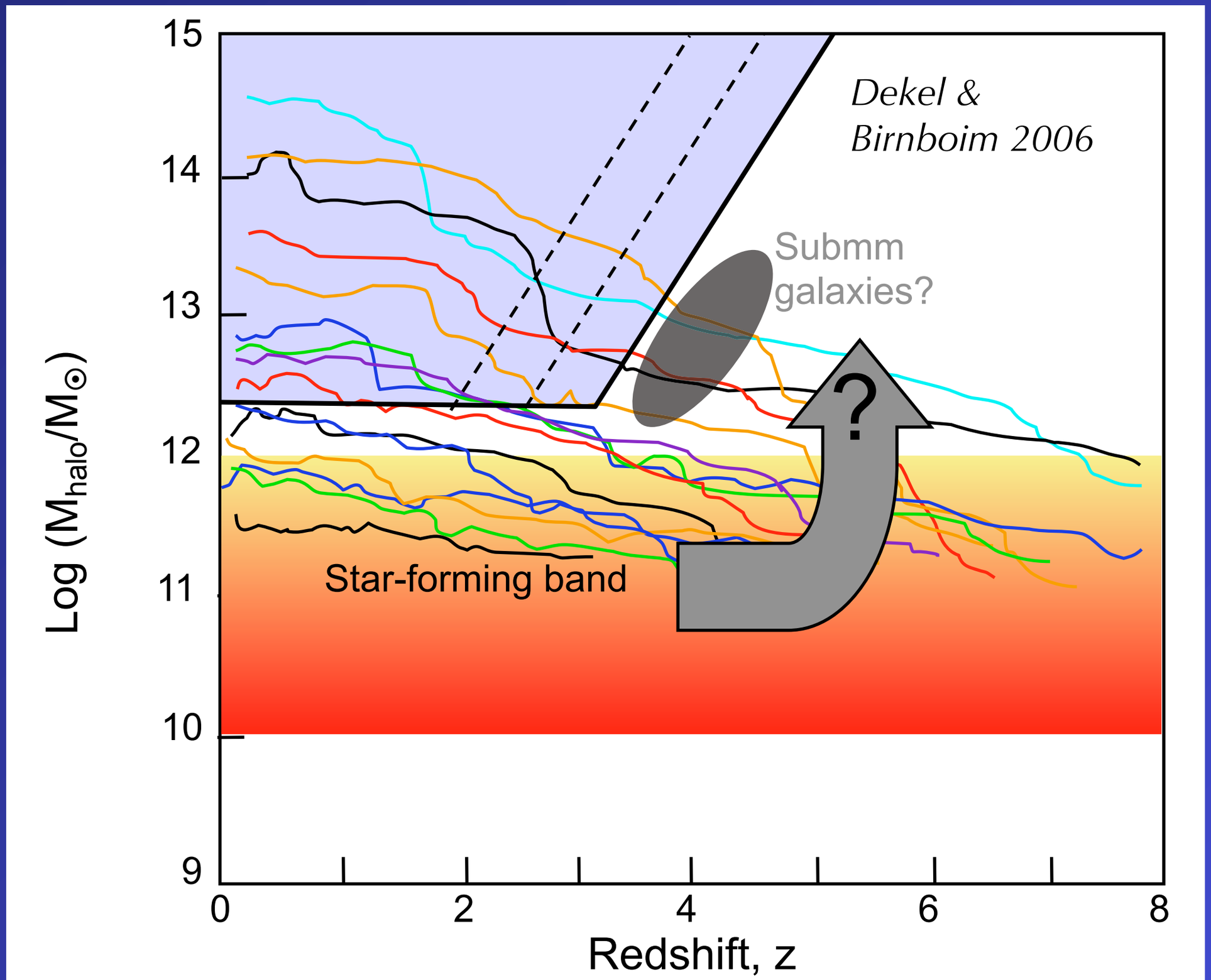

Flow through the color-mass diagram for “satellite” galaxies

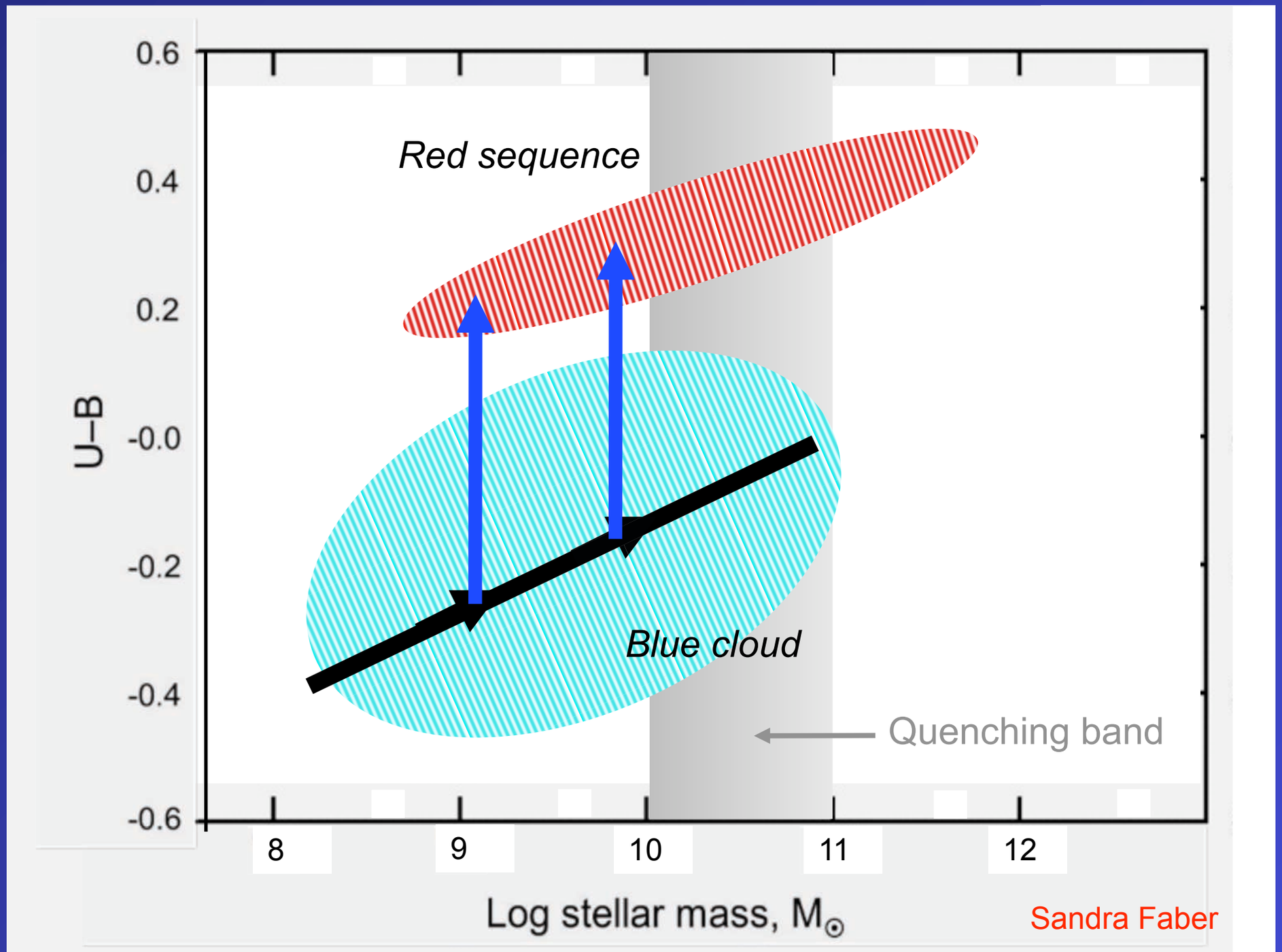

Sandra Faber

Flow through the color-mass diagram for “central” galaxies

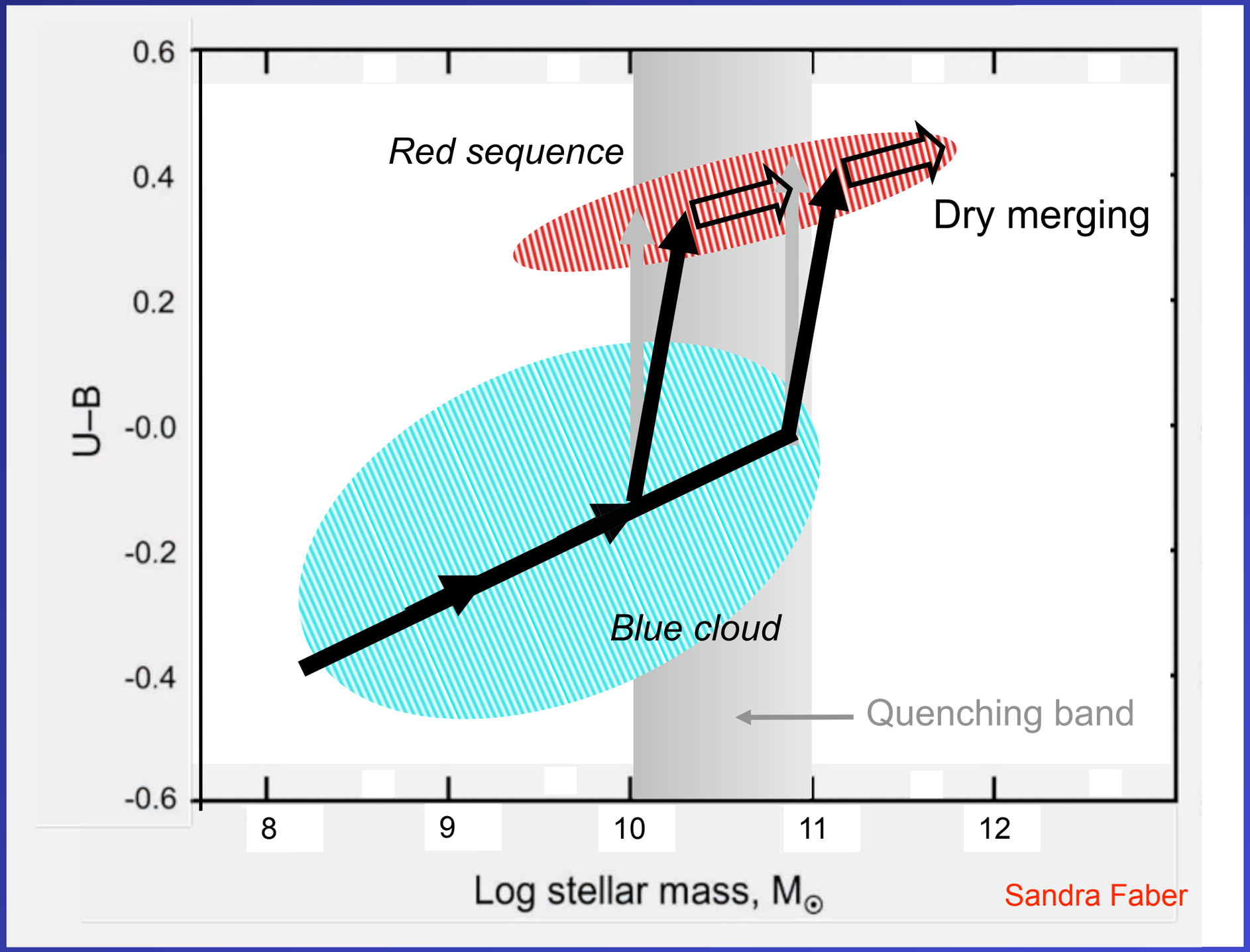

Sandra Faber

Flow through the CM diagram versus environment

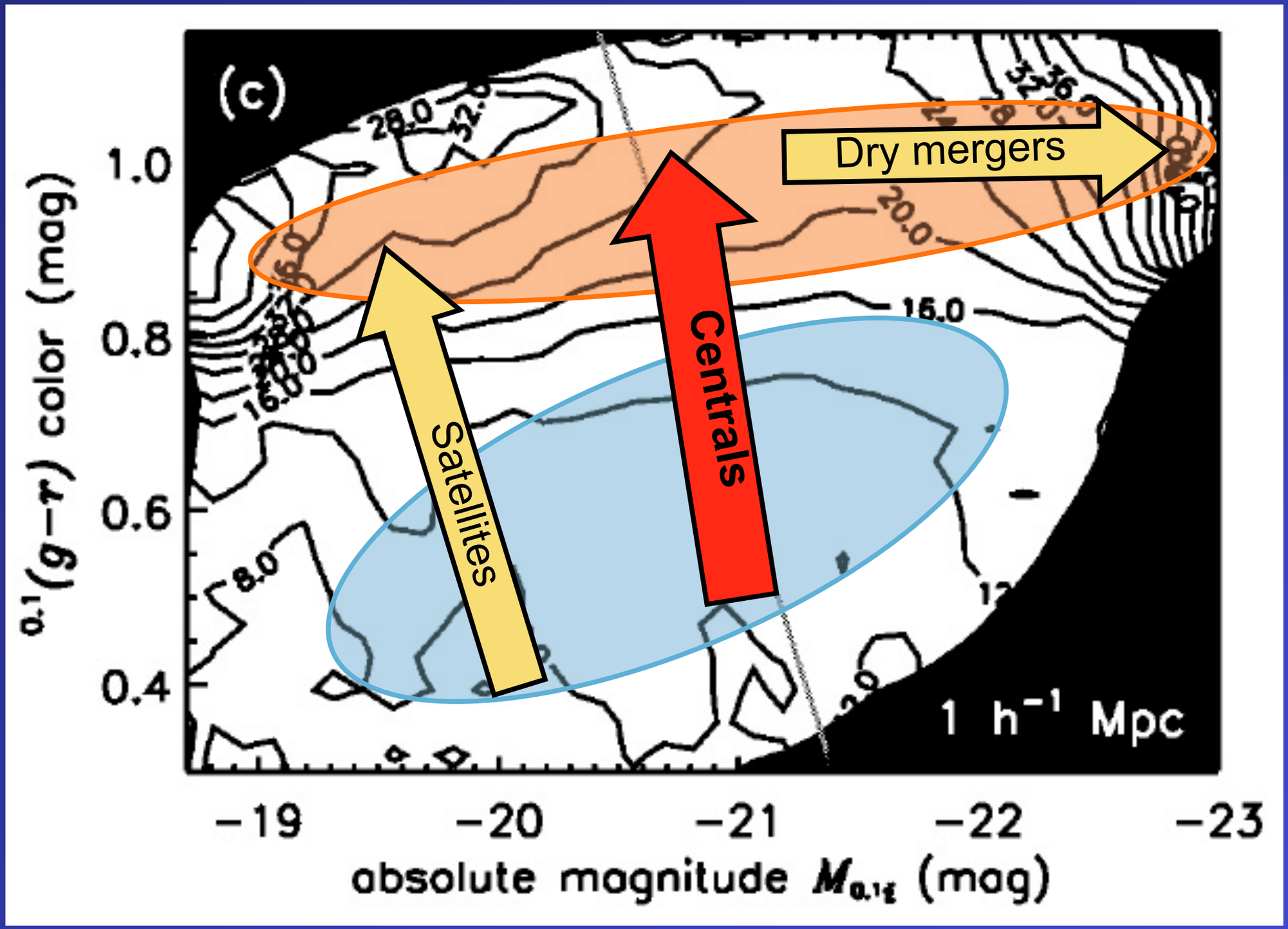

Sandra Faber

Hogg et al. 2003: Sloan Survey

Winter Quarter 2009 Joel Primack

Astronomy 233: Physical Cosmology

1. History of Observational Cosmology
2. General Relativity
3. Distances, Horizons
4. Boltzmann Equation: Neutrino Decoupling
5. Big Bang Nucleosynthesis, Recombination
6. Dark Matter Formation and Detection
7. Cosmic Microwave Background
8. Cosmic Inflation
9. After Inflation: Baryogenesis
10. Cosmic Web
11. Simulations and Semi-Analytic Models